Theoretical analysis of electronic structure of iron-sulfur clusters in hydrogenases

「ヒドロゲナーゼにおける鉄−硫黄クラスタの電子構造の理論解析」

２０１８

Kim Jaehyun

兵庫県立大学大学院生命理学研究科

Contents

Chapter 1
Introduction

To elucidate substantial mechanisms of biological functions, diverse methodologies such as experimental and computational/theoretical methods were required, and thus great efforts have been made to develop and apply such methodologies. Also, in order to experimentally elucidate 3D-structures of biological macromolecular systems, various experimental techniques such as Nuclear Magnetic Resonance (NMR) spectroscopy, X-ray crystallography, and Electron Microscope (EM) have been employed so far. Moreover, to analyze chemical properties of functional structures involved in biological macromolecules, further spectroscopic techniques such as Vibrational Spectroscopy, Electron Paramagnetic Resonance (EPR) spectroscopy, and Mossbauer spectroscopy have been required and employed.

However, it is too difficult to obtain comprehensive and detailed information, as well as fragmental data, concerning the electronic structures of biochemical reactions by employing such experimental diffraction and spectroscopic techniques. In addition, experimental results are suffered from serious errors due to their strict technical limitations. Thus, to reveal substantial roles and mechanisms of functional structures of biological systems, combined experimental and computational/theoretical methodologies are essentially important. For example, *ab initio* quantum mechanics (QM) calculation has been employed up to date, and have elucidated detailed electronic structures of biological molecular systems as well as chemical systems, as an

indispensable theoretical tool to analyze mechanisms coupled with those experimental techniques.

In this thesis, we take hydrogenase as an example of biological macromolecular systems of great interest. Hydrogenase catalyzes both uptake and evolution of hydrogen. Accordingly, hydrogenase has been expected to contribute to resolve the energy problem, which is a worldwide social issue as a great challenge for human being. Actually, the fossil fuel economy on which human being depends is unsustainable, because the growing economy has seriously relied on finite resources, which become irreversibly depleted. Moreover, consumption of fossil fuel increases the CO_2 level in an atmosphere, which has already raised a greenhouse effect on a global scale. For this situation, hydrogen has been proposed as an alternative fuel, because of an ecologically-friendly fuel for the future. Actually, hydrogen fuel has many advantages in comparison with fossil fuel; for example, hydrogen is a clean-burning fuel with high energy density and renewable, and we can generate it from water, which is a cyclical and sustainable process. However, in order to generate and split dihydrogen, expensive metals, such as platinum, have been employed as the catalysts, which is a serious problem in use of hydrogen as an alternative fuel.

However, hydrogenases, which are produced by many kinds of microorganisms to catalyze both dihydrogen (H_2) dissociation and association reactions ($H_2 \rightleftharpoons 2H^+ + 2e^-$), possess a catalytic active site with an abundant metal-binding cluster (e.g. Ni and Fe). Moreover, the turnover rate of the catalytic reaction is comparable with the catalysts that are employed in the commercial field. Owing to these advantages, hydrogenases attract many interests concerning the mechanism of the catalysis.

The aim of this work is to investigate the mechanisms of a particular hydrogenase that sustains its activity even in the presence of dioxygen (O_2), which is termed O_2-tolerance of hydrogenase, by elucidating the electronic structures of the transition metal-binding clusters of the hydrogenase. For this purpose, we employed *ab initio* QM calculations to analyze the functional role of the Fe-S clusters involved in hydrogenase. The analysis revealed that an experimentally-identified hydroxyl ion, for which the functional role remained to be unknown, modulated a frontier orbital of a Fe-S cluster located in the proximity of the active site, thereby creating electron transfer (ET) pathways through the transition metal-binding functional clusters. The present findings have experimentally been inaccessible, which shows that theoretical techniques combined with experimental data are indispensable to elucidate the mechanisms of biological macromolecular systems.

Chapter 2

Electronic structure analysis of [4Fe-3S] proximal cluster of hydrogenase employing *ab initio* electronic structure calculation

2-1. Introduction

Hydrogenases govern hydrogen metabolism, i.e., the uptake/evolution of dihydrogen, in the eubacterial world, including the inexpensive abundant metals of nickel and iron in their active sites.[1,2] The enzymatic reaction that hydrogenases catalyze is simple: $H_2 \rightleftharpoons 2H^+ + 2e^-$. From a technological viewpoint, H_2 evolution and oxidation for industrial applications are currently based on expensive metals such as platinum. Note here that the turnover rates of some hydrogenases are comparable with those of noble-metal catalysts.[3-5] Since H_2 has potential as a clean energy carrier and is expected to be used as an alternative to fossil fuels,[6] hydrogenases have also attracted much interest as alternatives to catalysts that include expensive metals.[7,8]

Hydrogenases are classified into three phylogenetically unrelated families, i.e., [FeFe], [NiFe], and [Fe] families, based on the metal composition of their catalytic center (Table S1 in the Supplementary Materials).[9-12] Upon O_2 exposure, hydrogenases show different characteristics. [FeFe]-hydrogenases are rapidly and irreversibly inactivated.[5,13] Although [Fe]-hydrogenase in the cell extract of *Methanogenic archaea* is also rapidly inactivated by O_2 exposure, the purified enzyme is stable and active.[14] Some types of [NiFe]-hydrogenases, such as membrane-bound [NiFe] hydrogenase (MBH), H_2-sensing regulatory [NiFe]-hydrogenase, soluble NAD^+-reducing

[NiFe]-hydrogenase, and [NiFeSe]-hydrogenase, exhibit the ability to recover from the O_2 exposure.[15] The standard [NiFe]-hydrogenases are inactivated upon O_2 exposure, and are thus referred to as the O_2-sensitive [NiFe]-hydrogenases. By contrast, MBHs sustain their catalytic activity even in the presence of O_2,[16] and are classified as O_2-tolerant [NiFe]-hydrogenases.[10,11,17,18]

Microorganism	Hydrogenase	O_2 tolerance
D. Gigas	Standard [NiFe] hydrogenase	**No**
D. vulgaris Miyazaki	Standard [NiFe] hydrogenase	**No**
Hydrogenovibrio marinus	Membrane-bound [NiFe] hydrogenase (MBH)	**Yes**
Ralstonia eutropha H16	Membrane-bound [NiFe] hydrogenase (MBH)	**Yes**
Ralstonia eutropha H16	H_2-sensing regulatory [NiFe] hydrogenase	**Yes**
Ralstonia eutropha H16	Soluble NAD^+-reducing [NiFe] hydrogenase	**Yes**
D. baculatum	[NiFeSe]	**Yes**

Table 2.1. Classification of [NiFe] hydrogenases.

More specifically, the standard [NiFe]-hydrogenases react with O_2, which leads to changes in the redox state to a "mixture" of the [NiFe] active site, referred to as Ni-A and Ni-B, while for MBHs, only the Ni-B state is formed. Here, the Ni-A state needs over 1 h to be recovered, together with an elevated temperature and a long reductive treatment. In contrast, the Ni-B state is activated within 1 min in the presence of H_2, which is a characteristic of MBHs as O_2-tolerant hydrogenases.[11] Since understanding of the O_2 tolerance mechanism is important to develop H_2 evolution systems, MBHs have also been intensively investigated from a technical viewpoint.

MBHs consist of two subunits, the large and small subunits (Figure 2.1a), which

harbor a [NiFe] active site and three Fe-S clusters, respectively. The three Fe-S clusters are called the proximal, medial, and distal clusters (Figure 2.1a)). These Fe-S clusters are involved in electron transfer (ET) relays from (to) the [NiFe] active site to (from) the outside of the enzyme (both directions were experimentally characterized, depending on the reaction driven in the [NiFe] active site, i.e. the uptake or evolution of H_2).[11] The structures of the [NiFe] active site, medial cluster, and distal cluster are identical for the standard [NiFe]-hydrogenases and MBHs, while the proximal clusters are not: in the standard [NiFe]-hydrogenases, four Fe ions and four S ions (i.e., [4Fe-4S]) comprise the proximal cluster, which is coordinated by four cysteine (Cys) residues, whereas in MBHs, four Fe ions and three inorganic sulfur ions ([4Fe-3S]) compose the proximal cluster, which is coordinated by six cysteine residues (Figure 2.1b, c).[15,19-21] Notably, the two numerary cysteine residues in MBHs are replaced with glycine (Gly) residues in the standard [NiFe]-hydrogenases.

Moreover, the crystal structures of MBHs showed that the Fe4 ion in the proximal cluster structurally deviated depending on the redox state (e.g. the reduced or super-oxidized state), as shown in Figure 2.1c and Figure 2.2. In the crystal structures of the reduced state, Fe4 forms covalent bonds with S_{Cys19}, S_{Cys20}, S1, and S3 (in this report, the residue numbering system is subjected to that of *Ralstonia eutropha* MBH,[21] and the numbers of amino acid residues in the large and small subunits are represented with and without the superscript L, respectively). By contrast, in the super-oxidized state, Fe4 was located closer to N_{Cys20} than in the reduced state, which thus led to formation of a covalent bond with N_{Cys20} in the super-oxidized state, instead of S3 in the reduced state.[15,19-21]

The O_2-tolerant mechanism of [NiFe] hydrogenases has been attributed to the

[4Fe-3S] proximal cluster, as follows. In the presence of O_2, the [4Fe-3S] clusters of MBHs are converted to the super-oxidized state (i.e., $[4Fe-3S]^{5+}$), and it has also been suggested that the super-oxidized state of the proximal cluster is related to the formation of the Ni-B state, which is rapidly reactivated under reducing conditions. Moreover, several previous studies have suggested that the O_2 tolerance of MBHs is derived from the two above-mentioned unprecedented geometrical features, i.e., the replacements of the two Cys residues with the Gly residues and the positional deviations of the Fe4 ion depending on the redox state.[20,22-24]

Very recently, another characteristic feature has been revealed for the MBH from *Ralstonia eutropha*: a hydroxyl ion (OH^-) was identified to be attached to Fe1 of the proximal cluster in the super-oxidized state (Figure 2.1b, c).[21,25] The presence of the hydroxyl ion was confirmed by the Raman spectroscopy and *ab initio* electronic structure calculations.[21,25] Although the attachment of the hydroxyl ion to Fe1 was not found in the crystal structures of *Hydrogenovibrio marinus* and *Escherichia coli* MBHs, it was suggested that the hydroxyl ion attached to Fe1 might also be present in these MBHs,[26] since the structures of the proximal clusters are fundamentally equivalent among *Ralstonia eutropha*, *Hydrogenovibrio marinus*, and *Escherichia coli* MBHs.

Thus, the functional roles of the hydroxyl ion have not yet been elucidated, even whether or not it is relevant to the O_2-tolerant mechanism. Accordingly, in this study, we focused on the analysis of the functional roles of the hydroxyl ion in the catalytic mechanisms based on the electronic structures of the proximal cluster. To achieve this, we conducted *ab initio* density functional theory (DFT) calculations of the proximal cluster of *Ralstonia eutropha* MBH, in the presence and absence of the hydroxyl ion. For the calculations, we first explored the optimum spin states of the [4Fe-3S] core

moiety in the proximal cluster in the presence and absence of the hydroxyl ion, employing the spin models based on the broken symmetry (BS) approach.[27] Then, by adopting the several plausible spin states obtained, we conducted *ab initio* DFT calculations of the proximal cluster, and thus identified the optimum spin states.

The present analysis showed that in the super-oxidized state, the attachment of the hydroxyl ion to Fe1 induced rearrangements of the electronic structures of the proximal cluster, thereby leading to delocalization of the possible functional orbitals, which are represented by the lowest unoccupied molecular orbital (LUMO) and singly occupied molecular orbital (SOMO). The obtained results further enabled us to identify ET pathways through the [NiFe] active site, the proximal cluster, and the medial cluster. In fact, the ET pathways that were identified by an empirical scheme were consistent with the above-mentioned properties obtained by our *ab initio* electronic structure calculations. In this manner, the hydroxyl ion may contribute to the generation of the ET pathways by bridging the orbitals composing the LUMO of the proximal cluster, thus driving the reaction cycle of the O_2-tolerant MBHs.
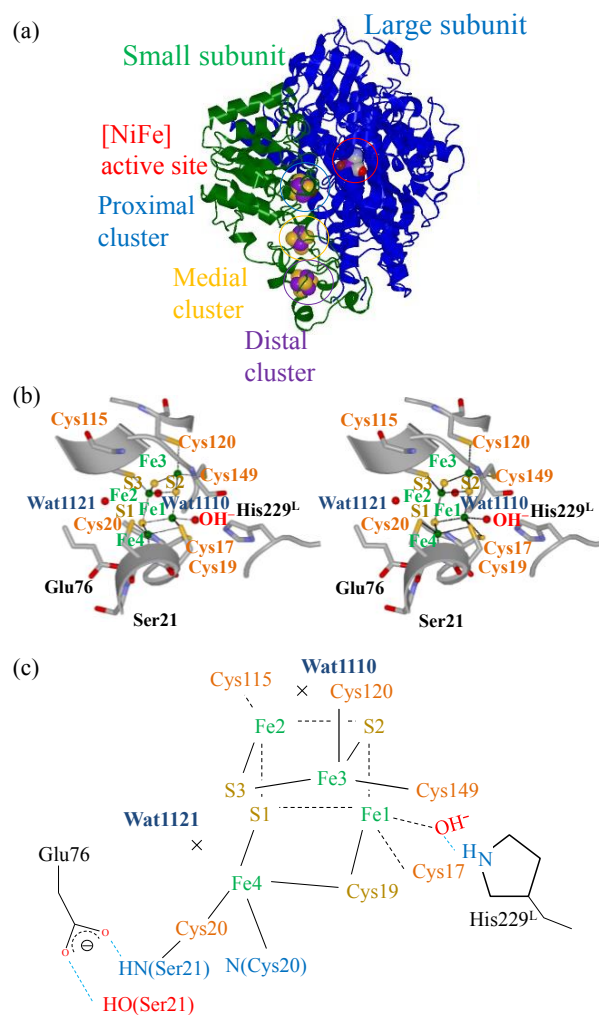
Figure 2.1. The crystal structure of *Ralstonia eutropha* MBH (PDB entry: 4IUD) and its [4Fe-3S] proximal cluster. (a) The overall structure of the MBH. The metal cofactors are represented by ball representation. The MBH is comprised of hetero dimer, and each monomer consists of the large and small subunits, which are colored blue and green, respectively. Red, blue, yellow, and violet circles show the positions of the [NiFe] active site, the proximal cluster, the medial cluster, and the distal cluster, respectively. (b) Stereo view of the proximal cluster. O atom that forms a covalent bond with Fe1 was suggested to be assigned to a hydroxyl ion in the previous experimental analyses. (c) Schematic representation of the proximal cluster in the super-oxidized state (Strc2).

11

In (b) and (c), the black broken lines show the covalent bonds in the [4Fe-3S] core and sulfur atoms that directly coordinate to Fe ions in the core moiety, and the blue broken lines show hydrogen bond.
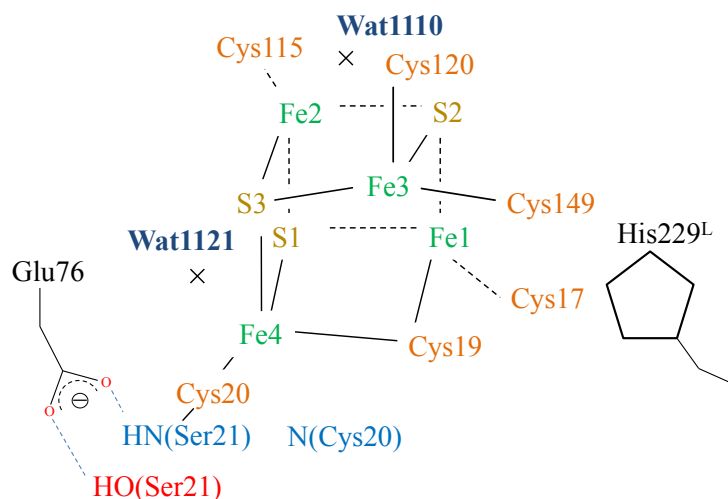

Figure 2.2. Schematic representation of the proximal cluster in the reduced state. The black broken lines show the covalent bonds in the [4Fe-3S] core structure. The sulfur atoms that directly coordinate to Fe ions in the core are also depicted. Hydrogen bonds are depicted by the blue broken lines.

2-2 Computational Methods

2-2-1 Model Building

For the quantum mechanics (QM) calculations, Models 1 and 2 (Figure. 2.3) were constructed, employing the atomic coordinates of the proximal cluster in the super-oxidized state of *Ralstonia eutropha* MBH in the absence and presence of the hydroxyl ion. To achieve this, the atomic coordinates represented by the Protein Data

Bank (PDB) entry 4IUD were adopted in this study. Also, the coordinates represented by 4IUC were employed to confirm the results of the calculations based on 4IUD.

Model 1 included the iron-sulfur cluster (i.e., [4Fe-3S]) and six Cys residues (i.e., Cys17, Cys19, Cys20, Cys120, Cys115, and Cys149) that coordinate to the Fe ions in the proximal cluster. Moreover, Ser21, Glu76, His229, two crystal water molecules that coordinate to the iron-sulfur cluster, and two peptide bonds between Cys19 and Cys20, and between Cys20 and Ser21 were included. Four cysteine residues (i.e., Cys17, Cys115, Cys120, and Cys149), Glu76, and His229 were truncated by replacing the C_α atoms with a methyl group ($-CH_3$). In Model 1 (101 atoms), the hydroxyl ion was removed, whereas it was contained in Model 2 (103 atoms).

2-2-2 Exploration of spin assignment

In the present analysis, for each of the iron and sulfur ions in the [4Fe-3S] proximal cluster, the charge would be Fe^{2+} or Fe^{3+}, and S^{2-}.[28] The formal charge of the [4Fe-3S] proximal cluster in the super-oxidized state was spectroscopically identified to be +5, and its total spin was +1/2.[28] Accordingly, the core is composed of Fe^{2+}, $3Fe^{3+}$, and $3S^{2-}$. For Fe^{2+} and Fe^{3+}, the high and low spins were used to construct possible spin combinations with a total spin of +1/2.
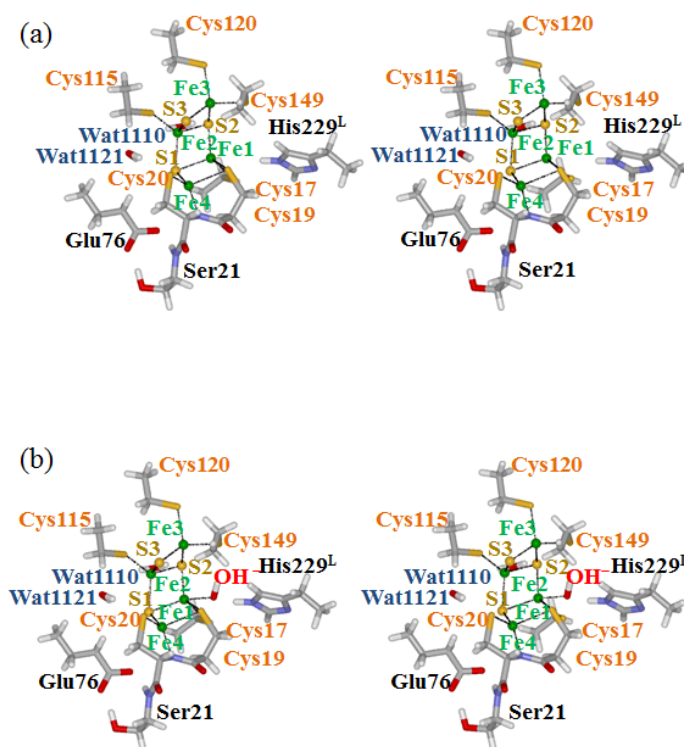
Figure 2.3. Structural models employed in our *ab initio* electronic structure calculations. The atomic coordinates of the proximal cluster were taken from the crystal structure of *Ralstonia eutropha* MBH (PDB entry: 4UID) to evaluate the super-oxidized state (the coordinates of the proximal cluster from the PDB entry 4UIC was also employed to confirm the calculated data). (a) Model 1 (101 atoms) does not include the hydroxyl ion, while (b) Model 2 (103 atoms) does.

Here, to generally describe the spin states of iron ions, A, B, and C are used for $3Fe^{3+}$ and D is used for Fe^{2+}. The possible spin combinations were classified into three groups, $A \neq B \neq C \neq D$, $A = B \neq C \neq D$, and $A = B = C \neq D$, and the numbers of possible spin combinations were 16, 48, and 16, respectively. Note that each spin combination involves some distinct spin assignments that are varied among the four Fe ions (i.e., Fe1, Fe2, Fe3, and Fe4). Thus, for each spin combination, the numbers of the spin

assignments are 24, 12, and 4 for A≠B≠C≠D, A=B≠C≠D, and A=B=C≠D, respectively. Accordingly, the total numbers of spin assignments are 384, 576, and 64 for A≠B≠C≠D, A=B≠C≠D, and A=B=C≠D, respectively. Thus, for the [4Fe-3S] cluster, the total number of spin assignments is 1024, and all the assignments are considered in the following analysis (Table 2.2).

The experimentally observed spin state, +1/2, was introduced to identify the optimum spin state of the proximal cluster in the super-oxidized state. In the [4Fe-3S] proximal cluster, Fe2, Fe3, and Fe4 form a tetrahedral structure, while Fe1, the O atom of the hydroxyl ion, S_{Cys19}, S_{Cys17}, S1, and S2 form a bipyramidal structure. In the present study, small models that include only the core atoms (i.e., Fe1, the O atom of the hydroxyl ion, S_{Cys19}, S_{Cys17}, S1, and S2) in the presence and absence of the OH^- were built, and then the energies of these models were also evaluated, which revealed that the optimum spin states were composed of high spin states of Fe ions, as previously shown experimentally.[29]

(a)

A≠B≠C≠D

A	B	C	D
Fe(III)	Fe(III)	Fe(III)	Fe(II)
5/2	−5/2	1/2	4/2
5/2	−5/2	1/2	−4/2
5/2	−5/2	1/2	2/2
5/2	−5/2	1/2	−2/2
5/2	−5/2	−1/2	4/2
5/2	−5/2	−1/2	−4/2
5/2	−5/2	−1/2	2/2
5/2	−5/2	−1/2	−2/2
1/2	−1/2	5/2	4/2
1/2	−1/2	5/2	−4/2
1/2	−1/2	5/2	2/2
1/2	−1/2	5/2	−2/2
1/2	−1/2	−5/2	4/2
1/2	−1/2	−5/2	−4/2
1/2	−1/2	−5/2	2/2
1/2	−1/2	−5/2	−2/2

(b)

A=B≠C≠D

A	B	C	D
Fe(III)	Fe(III)	Fe(III)	Fe(II)
5/2	5/2	−5/2	4/2
5/2	5/2	−5/2	−4/2
5/2	5/2	−5/2	2/2
5/2	5/2	−5/2	−2/2
5/2	5/2	1/2	4/2
5/2	5/2	1/2	−4/2
5/2	5/2	1/2	2/2
5/2	5/2	1/2	−2/2
5/2	5/2	−1/2	4/2
5/2	5/2	−1/2	−4/2
5/2	5/2	−1/2	2/2
5/2	5/2	−1/2	−2/2
−5/2	−5/2	5/2	4/2
−5/2	−5/2	5/2	−4/2
−5/2	−5/2	5/2	2/2
−5/2	−5/2	5/2	−2/2
−5/2	−5/2	1/2	4/2
−5/2	−5/2	1/2	−4/2
−5/2	−5/2	1/2	2/2
−5/2	−5/2	1/2	−2/2
−5/2	−5/2	−1/2	4/2
−5/2	−5/2	−1/2	−4/2
−5/2	−5/2	−1/2	2/2
−5/2	−5/2	−1/2	−2/2
1/2	1/2	5/2	4/2
1/2	1/2	5/2	−4/2
1/2	1/2	5/2	2/2
1/2	1/2	5/2	−2/2
1/2	1/2	−5/2	4/2
1/2	1/2	−5/2	−4/2
1/2	1/2	−5/2	2/2
1/2	1/2	−5/2	−2/2
1/2	1/2	−1/2	4/2
1/2	1/2	−1/2	−4/2
1/2	1/2	−1/2	2/2
1/2	1/2	−1/2	−2/2
−1/2	−1/2	5/2	4/2

(c)

A=B=C≠D

A	B	C	D
Fe(III)	Fe(III)	Fe(III)	Fe(II)
5/2	5/2	5/2	4/2
5/2	5/2	5/2	−4/2
5/2	5/2	5/2	2/2
5/2	5/2	5/2	−2/2
−5/2	−5/2	−5/2	4/2
−5/2	−5/2	−5/2	−4/2
−5/2	−5/2	−5/2	2/2
−5/2	−5/2	−5/2	−2/2
1/2	1/2	1/2	4/2
1/2	1/2	1/2	−4/2
1/2	1/2	1/2	2/2
1/2	1/2	1/2	−2/2
−1/2	−1/2	−1/2	4/2
−1/2	−1/2	−1/2	−4/2
−1/2	−1/2	−1/2	2/2
−1/2	−1/2	−1/2	−2/2

Table 2.2. Possible spin combinations of four Fe ions in the [4Fe-3S] core moiety, where one is Fe^{2+} and the other three are Fe^{3+}. A, B, C, and D show the spin state of each Fe ion. The spin combinations are classified into (a) A≠B≠C≠D, (b) A=B≠C≠D, and (c) A=B=C≠D.

This result obtained by our *ab initio* calculations of small models can be understood as follows (Figure 2.4). In the ideal trigonal bipyramidal structure, the energy levels of d_{zx} and d_{xy} are identical to those of d_{yz} and $d_{x^2-y^2}$, while those of d_{xy} and

$d_{x^2-y^2}$ are larger than those of d_{yz} and d_{zx}, respectively (the energy level of d_{z^2} is the highest). If the energy gaps among these three energy levels are lower than the spin pairing energy, Fe^{2+} and Fe^{3+} may exhibit high spins of 4/2 and 5/2, respectively. This spin configuration inferred above is fundamentally consistent with the above-mentioned calculations employing our small models.
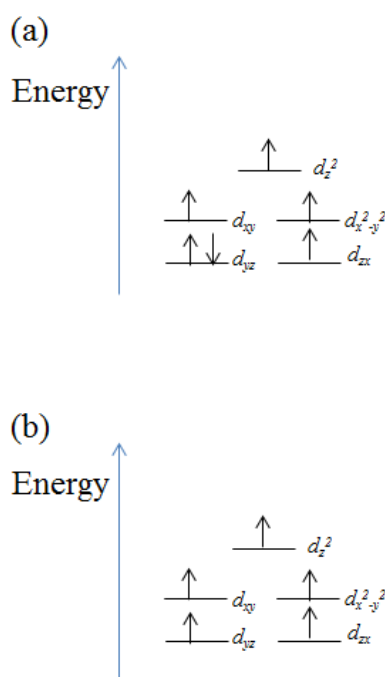

Figure 2.4. Electron arrangements in $3d$ orbital of Fe^{2+} (a) and Fe^{3+} (b) in the trigonal bipyramidal structure.

Thus, all the Fe ions can be assumed to be in their high spin states, and so the combinations of the spin states of the four Fe ions are restricted; i.e., two Fe ions are +5/2 and the others are −4/2 and −5/2. As a consequence, 12 possible spin assignments

were acceptable, and thus the energies of all the possible spin states of the proximal cluster were evaluated by *ab initio* electronic structure calculations of both Models 1 and 2 coupled with the geometry optimization of H atoms (the details are mentioned below) (Table 2.3).

	Fe1	Fe2	Fe3	Fe4
BS12	−4/2	−5/2	5/2	5/2
BS21	−5/2	−4/2	5/2	5/2
BS13	−4/2	5/2	−5/2	5/2
BS31	−5/2	5/2	−4/2	5/2
BS14	−4/2	5/2	5/2	−5/2
BS41	−5/2	5/2	5/2	−4/2
BS23	5/2	−4/2	−5/2	5/2
BS32	5/2	−5/2	−4/2	5/2
BS24	5/2	−4/2	5/2	−5/2
BS42	5/2	−5/2	5/2	−4/2
BS34	5/2	5/2	−4/2	−5/2
BS43	5/2	5/2	−5/2	−4/2

Table 2.3. 12 types of spin states analyzed in the present study, that were to the [4Fe-3S] core in the super-oxidized states. These spin states were selected from 1,024 spin states in the spin assignments, restricted by the previous experimental data on the total charge and spin state of the proximal cluster. To give the spin states of the proximal cluster ($S = 1/2$), the negative spins, −4/2 [Fe(II)] and −5/2 [Fe(III)], were assigned to Fei and Fej, respectively, which is referred to here as BSij.

To specify the spin assignments of the [4Fe-3S] cluster, the nomenclature BSij is

employed: BS is an abbreviation of the broken symmetry state, and i and j indicate the (serial) numbers of Fe ions to which $-4/2$ and $-5/2$ were assigned, respectively.[15] For example, BS12 indicates that Fe1 and Fe2 are $-4/2$ and $-5/2$, respectively (accordingly, the spin assignments of Fe3 and Fe4 are $+5/2$). Thus, for BS12, the spin assignment of the Fe ions is described as (Fe1, Fe2, Fe3, Fe4) = $(-4/2, -5/2, +5/2, +5/2)$, for which the total spin is 1/2. Thus, to identify the optimal spin state of the [4Fe-3S] proximal cluster, ab initio electronic structure calculations were conducted for the 12 spin assignments for both Models 1 and 2, as mentioned above.

2-2-3 Quantum mechanics calculation

All the QM calculations were performed by employing Gaussian09,[30] and the all-electron hybrid spin-unrestricted Hartree−Fock (UHF)/DFT scheme was adopted with the B3LYP functional2[31,32] For Models 1 and 2, the triple-ζ valence polarized (TZVP) basis set[33,34] was applied to the Fe ions and the atoms that directly coordinate to the Fe ions. For the other atoms, the 6-311G** basis set[35] was adopted. For each QM calculation, geometry optimization was performed with all hydrogen atoms being movable.

2-2-4 Orbital analysis

In our orbital analysis, to investigate the contribution of a certain atomic orbital in an MO, the square of its coefficient C_i^j was employed, where i and j are the numbers of the basis function and the MO, respectively. C_i^{HOMO} and C_i^{LUMO} were also employed to indicate coefficients associated with the HOMO and LUMO, respectively.

2-2-5 Analysis of ET pathway

In order to investigate possible ET pathways by an empirical method, we employed the *pathways* plugin for VMD.[36,37] The ET reaction rate (k_{ET}) is described as the following function under a high-temperature and non-adiabatic condition.[38]

$$k_{ET} = \frac{2\pi}{h} \frac{1}{\sqrt{4\pi\lambda k_B T}} |T_{DA}|^2 \exp\left[-\frac{(\Delta G + \lambda)^2}{4\lambda k_B T}\right]$$

ΔG, λ, and T_{DA} are the reaction free energy, the reorganization energy, and the electronic donor-to-tunneling coupling, respectively. k_B is Boltzmann's constant and $\hbar$ is Planck's constant divided by 2π. T_{DA} is employed to evaluate the candidates of ET pathways.[38] The strategy of *pathways* is to find the pathways that exhibit high T_{DA}.[38]

$$T_{DA} = A \prod_i \varepsilon_i^{C-bond} \prod_j \varepsilon_j^{H-bond} \prod_k \varepsilon_k^{space}$$

A is a prefactor. ε^{C-bond}, ε^{H-bond}, and ε^{space} are the penalties of the steps meditated by a covalent bond, a hydrogen bond, and a space, respectively. $\varepsilon^{C-bond} = 0.6$ is set on the basis of the experiments of Closs and Miller.[39] The penalties of the steps through a hydrogen bond and a space are given by $\varepsilon^H = (\varepsilon^C)^2 \exp[-\beta^S(R^H - 2.8)]$ and $\varepsilon^S = \varepsilon^C \exp[-\beta^S(R^S - 1.4)]$, respectively. R^H is the length between heavy atoms that generate a hydrogen bond in Å.[37] R^S is the length between heavy atoms that mediate the ET pathway without a hydrogen bond or a covalent bond. β^S, which is 1.1 Å^{-1}, is the decay cofactor for an empty space.[40]

2-3 Results and Discussion

Very recently, crystallographic and spectroscopic analyses have shown that a

hydroxyl ion (OH⁻) is attached to Fe1 in the proximal cluster of *Ralstonia eutropha* MBH.[21] It was proposed that in other MBHs, such as *Hydrogenovibrio marinus* and *Escherichia coli* MBHs, the hydroxyl ion might also be present in their proximal clusters. Anyway, the hydroxyl ion has not been observed so far except for in *Ralstonia eutropha* MBH, although the structures of the proximal clusters are almost identical among these MBHs. Moreover, despite intensive studies, the functional roles of the hydroxyl ion identified in *Ralstonia eutropha* MBH have not yet been established.

In this study, we investigated the electronic structures of the proximal cluster in the presence and absence of the hydroxyl ion, and thereby analyzed its effects on the electronic structure of the proximal cluster. For comparison, we extracted the iron-sulfur cluster from the crystal structure and constructed two structural models, in which the OH⁻ was removed and included (Models 1 and 2, respectively). Then, we identified the possible spin assignments by considering the total charge and spin state of the proximal cluster, which were experimentally measured, as the restrains in our BS approach (Table 2.3).

2-3-1 Exploration of optimum spin assignment of Fe ions in [4Fe-3S] cluster

For all the possible spin assignments in Models 1 and 2 (Table I), we calculated the total energy values by *ab initio* electronic structure calculation. In Model 1, BS12, BS21, BS13, and BS31 exhibited energies that were at least 9.45 kcal/mol lower than those of the other spin assignments (Figure 2.5a). By contrast, the energy differences among BS12, BS21, BS13, and BS31 were smaller than 2.04 kcal/mol, and thus these four spin assignments were clearly distinguished from the others in terms of the total energy. Thus, these four spin assignments are favorable for the proximal cluster in the absence

of the hydroxyl ion.

In Model 2, BS12, BS21, BS34, and BS43 exhibited the total energy values that were at least 5.16 kcal/mol smaller than the others (Figure 2.5b). In contrast, the energy differences among BS12, BS21, BS34, and BS43 were less than 2.89 kcal/mol, and thus were clearly distinguished from the others in terms of the total energy. Accordingly, these four spin assignments are favorable for the proximal cluster in the presence of the hydroxyl ion. In a previous study where DFT calculations of the proximal cluster were performed with the hydroxyl ion, BS12 was adopted as the spin state, which is consistent with one of our favorable spin states of Model 2, although the detailed conditions employed in the calculations were different (for example, the basis set used in the previous calculations was not equivalent to that in the present analysis, the latter being a more advanced one).[21] Thus, the analysis indicated that the attachment of the hydroxyl ion to Fe1 induced the change in the optimal spin assignment of the proximal

Note that in the previous studies, BSij and BSji were shown to be identical by ab initio calculations of three Fe-S clusters (i.e., [2Fe2S], [3Fe4S], and [4Fe4S]).[41,42] However, this equivalence of BSij and BSji was not necessarily the case in the present study, since the [4Fe-3S] proximal clusters in MBHs are distorted compared with the standard iron-sulfur clusters as were analyzed in the previous studies. Moreover, in Model 2, a hydroxyl ion is attached to Fe1, which leads to distinct electronic structures compared from those of the standard iron-sulfur clusters, as indicated below. Thus, in the present analysis, it is not clear that BSij and BSij are equivalent in terms of the electronic structure and spin state. In fact, for Model 1, the lower-energy spin assignments, i.e., BS12 and BS21, exhibited almost equivalent energy (Figure 2.5a), whereas for Model 2, even the lower-energy spin assignments, i.e., BS34 and BS43, exhibited energies that

were different by 1.77 kcal/mol. Moreover, for both Models 1 and 2, most spin assignments with higher energies show distinct energy values for BSij and BSji. Thus, the present analysis indicated that the assumption that BSij and BSji are equivalent in the electronic structure cannot be adopted in Model 2 even for the optimal spin states.
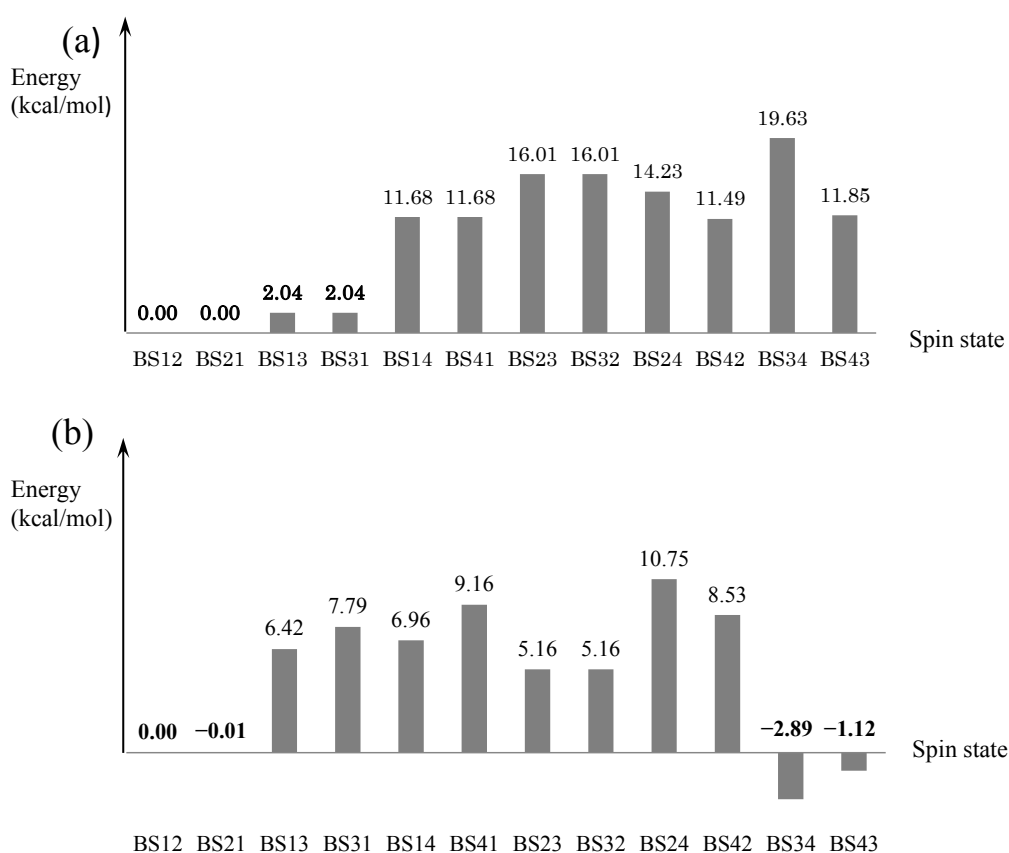

Figure 2.5. The relative energy values of the 12 distinct types of spin assignments in Models 1 and 2, with respect to the energy value of BS12 as the reference (i.e., 0 kcal/mol). In (a) Model 1, BS12 and BS21, for which the energy values are almost identical, are the most stable spin states. In (b) Model 2, BS34 is the most favorable spin state, but the energy values of BS43, BS12, and BS21 are comparable with that of BS34.

2-3-2 Electronic structure analysis

2-3-2-1 Frontier orbitals

We investigated the differences in the electronic structures of the proximal cluster in the presence and absence of the hydroxyl ion. For the HOMOs, the ratios of the $3d$ orbitals of Fe4 were significantly different between Model 1 (BS12 and BS13) and Model 2 (BS12 and BS34). In fact, for the $3d$ orbitals of Fe4, the sums of the square values of each coefficient C_i^{HOMO} were as small as 0.0047 and 0.0026 in the HOMOs of BS12 and BS13 of Model 1, respectively (Table 2.4). By contrast, for Model 2, the corresponding values for the $3d$ orbitals of Fe4 were 0.2200 and 0.3798 in the HOMOs of BS12 and BS34, respectively (Table 2.4). Thus, the attachment of the hydroxyl ion significantly increased the ratios of the $3d$ orbitals of Fe4 in the HOMOs of the proximal cluster.

For the LUMOs, the $3d$ orbitals of Fe4 and the $3p$ orbitals of S atoms were significantly different in terms of the ratios involved in Model 1 (BS12 and BS13) and Model 2 (BS12 and BS34) (Table 2.4). First, for the $3d$ orbitals of Fe4 in Model 1, the sums of the $C_i^{\mathrm{LUMO}\,2}$ values were 0.4807 and 0.4830 in BS12 and BS13, whereas in Model 2, those in BS12 and BS34 were as small as 0.1113 and 0.0166, respectively. Second, for the $3p$ orbitals of S_{Cys17} and S_{Cys19} in Model 1, the sums of the $C_i^{\mathrm{LUMO}\,2}$ values were markedly lower than those in Model 2 (Table 2.4). Moreover, for the hydroxyl ion (i.e., Model 2), considerable amounts of $2p$ orbitals of the O atom were revealed to be involved in the LUMOs for both BS12 and BS34; in fact, for the $2p$ orbitals of the O atom, the sums of the $C_i^{\mathrm{LUMO}\,2}$ values were 0.1884 and 0.2790,

respectively. Such involvement of the $2p$ orbitals of the hydroxyl ion may perturb the LUMOs of the proximal cluster (as discussed below).

	Atom	Model 1			Model2		
		Orbital	BS12	BS13	Orbital	BS12	BS34
HOMO	Fe4	S. d	0.0047	0.0026	S. d	0.2200	0.3798
	S_{Cys17}	S. p	0.0172	0.1742	S. p	0.0413	0.0102
	S_{Cys19}	S. p	0.0017	0.0985	S. p	0.0496	0.0040
	S_{Cys20}	S. p	0.0181	0.0155	S. p	0.0477	0.1059
	O_{OH-}	S. p	-	-	S. p	0.0453	0.0055
LUMO	Fe4	S. d	0.4807	0.4830	S. d	0.1113	0.0166
	S_{Cys17}	S. p	0.0002	0.0002	S. p	0.0387	0.1017
	S_{Cys19}	S. p	0.0125	0.0114	S. p	0.3617	0.3243
	S_{Cys20}	S. p	0.0504	0.0372	S. p	0.0114	0.0116
	O_{OH-}	S. p	-	-	S. p	0.1884	0.2790

Table 2.4. S.d and S.p represent the sums of $C_i^{HOMO\,2}$ and $C_i^{LUMO\,2}$ values of the valence orbitals in each atom. O is oxygen atom of the hydroxyl ion.

Accordingly, we concluded that the hydroxyl ion significantly affects the electronic structure of the [4Fe-3S] proximal cluster. So, we further examined the effects of the hydroxyl ion on the spatial distributions of the frontier orbitals (Figures 2.6 and 2.7). The HOMOs in BS12 and BS13 of Model 1 were distributed on Fe ions (Fe1, Fe2, and Fe3), S ions (S1, S2, and S3), and S atoms of Cys residues coordinating to Fe ions, which are S_{Cys17}, S_{Cys20}, S_{Cys115}, S_{Cys120}, and S_{Cys149} for BS12 and these five S atoms plus S_{Cys19} for BS13. Notably, the $3d$ orbitals of Fe4 were marginally included in the HOMOs of Model 1. In Model 2, the HOMOs in BS12 and BS34 were further

distributed on Fe ions (Fe1, Fe2, Fe3, and Fe4), but were less distributed on the regions composed of the Cys residues and S ions than those of Model 1. Note that the $3d$ orbitals of Fe4 were clearly more involved in the HOMOs of Model 2 than in those of Model 1, which thereby resulted in the HOMOs of Model 2 tending to localize around Fe4. Thus, the distributions of the HOMOs were different between Models 1 and 2.

The LUMOs of Model 1 (BS12 and BS13) primarily included the $3d_{z2}$ orbitals of Fe4 and the $3p_z$ orbitals of S_{Cys20}, and thus were localized on these central core atoms of the proximal cluster (Figure 2.7a, b and Figure 2.8a, b). In the previous study performed by Volbeda et al., the LUMO in BS13 was demonstrated,[15] which was very similar to that of Model 1 in the present study. Thus, in the absence of the hydroxyl ion, the localization of the LUMOs was confirmed.

By contrast, in Model 2 (BS12 and BS34), the LUMOs were most commonly observed on S_{Cys17}, S_{Cys19}, S_{Cys20}, N_{Cys20}, and the O atom of the hydroxyl ion, and also appeared on Fe1, Fe3, and Fe4 for BS12 and on Fe1, Fe2, and Fe4 for BS34 (Figure 2.7c, d and Figure 2.8c, d). As a consequence, it was shown that the attachment of the hydroxyl ion induces the delocalization of the LUMOs, whereas it is likely to make the HOMOs localized around Fe4, as mentioned above. This was also confirmed by comparing the LUMOs of Models 1 and 2 (in the BS12 and BS34 spin states, respectively), where the atomic coordinates of 4IUD was employed, with the LUMOs obtained employing the modeled structures (corresponding to Models 1 and 2), where the coordinates of 4IUC were employed. The analysis indicated that the resultant LUMOs obtained from the 4IUC and 4IUD coordinates were equivalent.
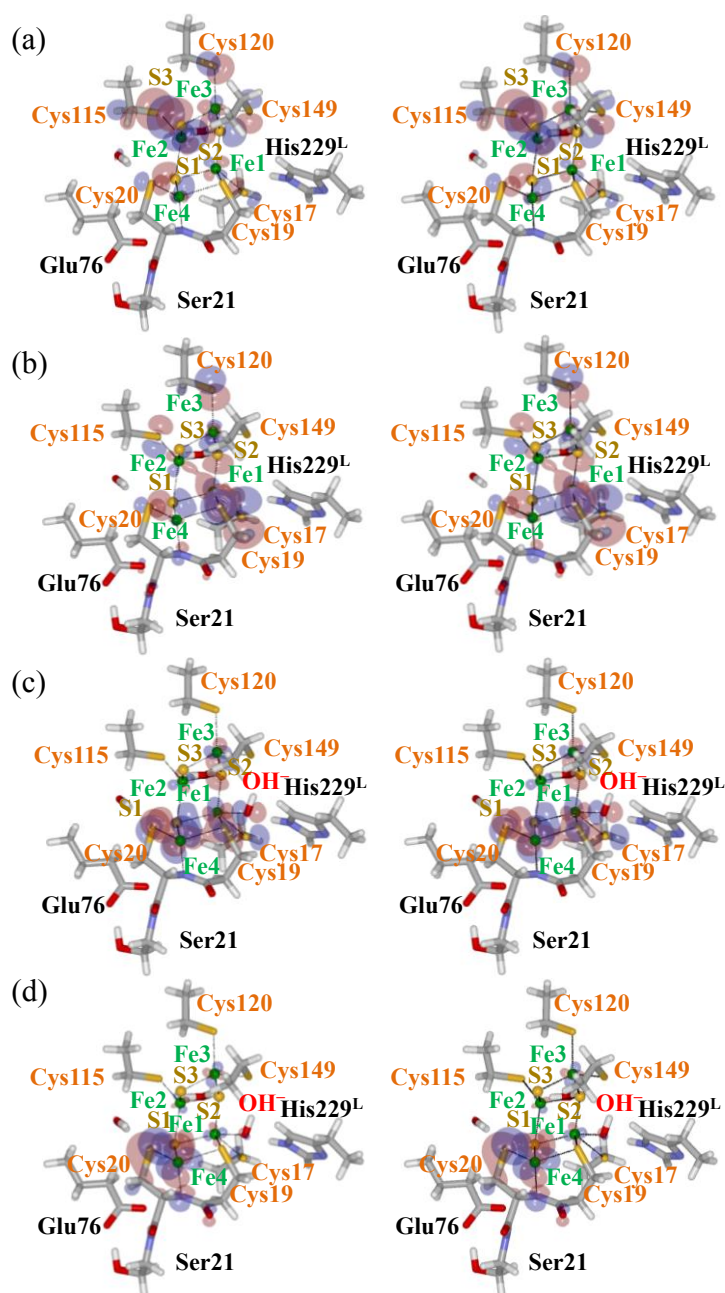
Figure 2.6. (Color online) HOMOs for the optimal spin states of Models 1 and 2. The HOMOs are shown; i.e., (a) BS12 and (b) BS13 in Model 1, and (c) BS12 and (d) BS34 in Model 2. The HOMOs in BS12 and BS13 for Model 1 are commonly observed on the Cys residues coordinating to Fe ions, S1, S2, S3, Fe1, Fe2, and Fe3, while only a small amount of orbitals are located on Fe4. In Model 2, the HOMOs in BS12 and BS34 are less distributed on the Cys residues and sulfur ions, but are clearly more located on Fe1, Fe2, Fe3, and Fe4. Note here that in Model 2, the HOMO distribution on Fe4 is larger than that in Model 1. The contour level used to render the orbitals is 0.015.
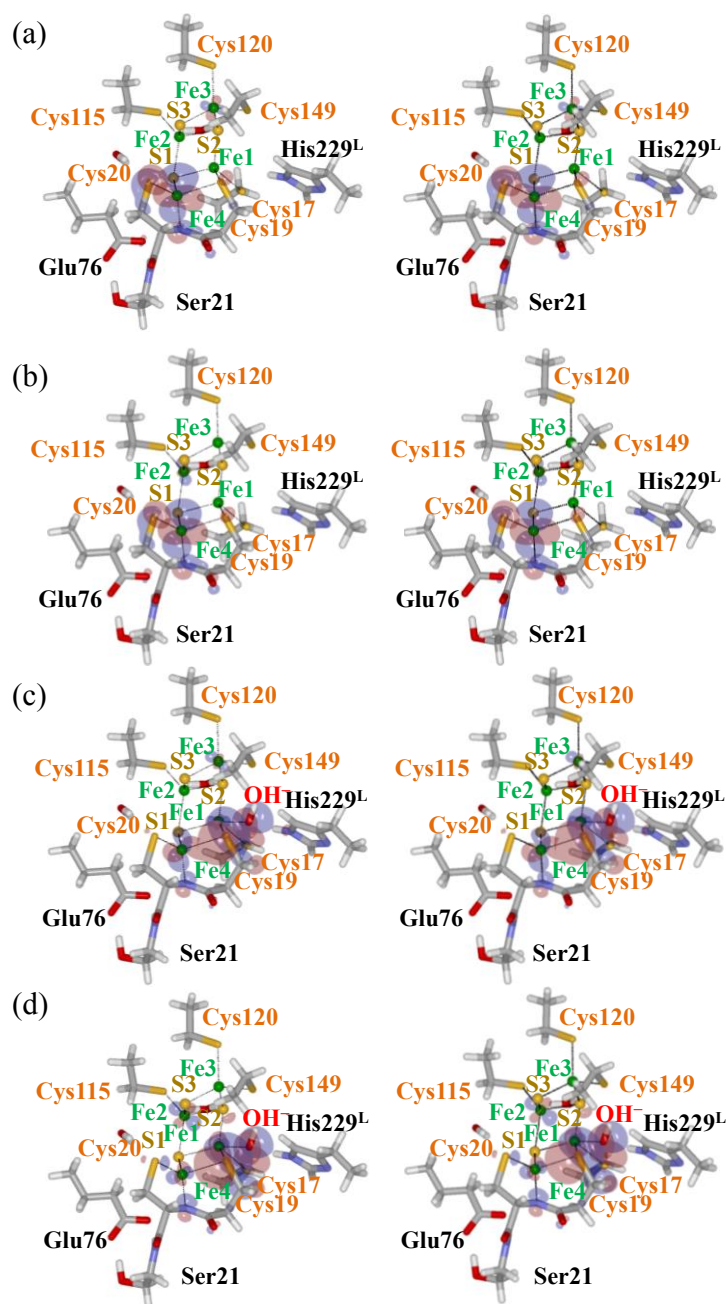
Figure 2.7. The LUMOs in terms of the optimal spin states of Models 1 and 2. In (a) BS12 and (b) BS13 of Model 1, the LUMOs are localized on Fe4 ion and S_{Cys20}. In contrast, in (c) BS12 and (d) BS34 of Model 2, the LUMOs are delocalized as follows: In BS12, the LUMO is mostly composed of S_{Cys17}, S_{Cys19}, the hydroxyl ion, Fe1, Fe3, and Fe4. In BS34, the LUMO is principally composed of S_{Cys17}, S_{Cys19}, S_{Cys20}, N_{Cys20}, the hydroxyl ion, Fe1, Fe2, and Fe4. The contour level to render the orbitals is 0.015.
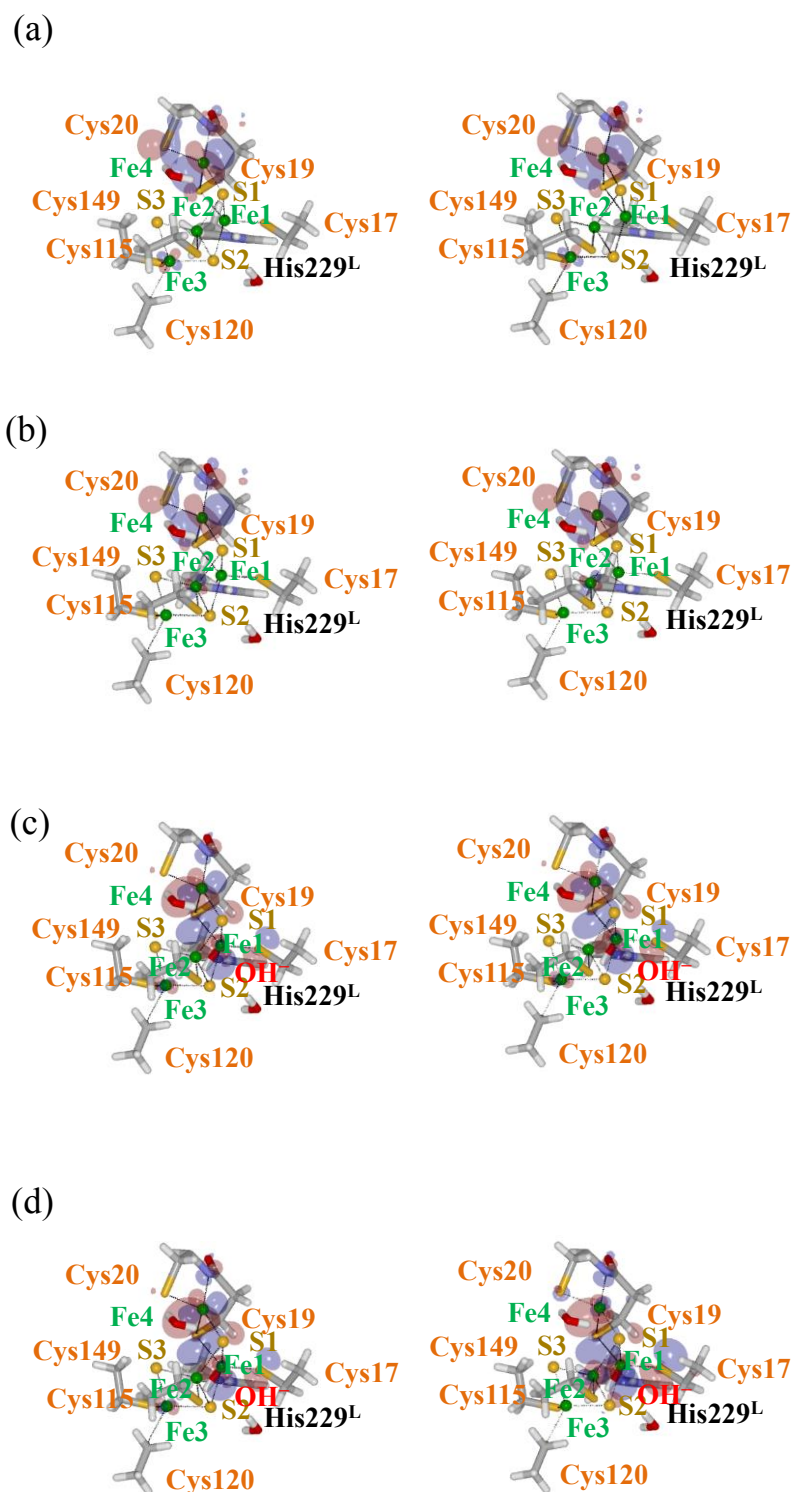
Figure 2.8. The LUMOs of Model 1 in BS12 (a) and BS13 (b), and those of Model 2 in BS12 (c) and BS34 (d), all of which are viewed from another direction that is different from that of Figure 2.7, to provide distinct perspectives of the LUMOs. The contour level to render the orbitals is 0.015. Also see Figure 2.1b, c.

2-3-2-2 HOMO-LUMO energy gap

The differences in the HOMO-LUMO energy gaps were marginal in Models 1 and 2. In Model 1, the HOMO-LUMO energy gaps of BS12 and BS13 were 50.27 and 50.16 kcal/mol, respectively (Figure 2.9a, b), and in Model 2, those of BS12 and BS34 (i.e., 38.84 and 40.61 kcal/mol, respectively) (Figure 2.9c, d) were slightly smaller than the above-mentioned values of Model 1. Although the HOMO-LUMO energy gaps thus decreased by ~10 kcal/mol through the attachment of the hydroxyl ion, the values were still large. Thus, the effect of the hydroxyl ion on the HOMO-LUMO energy gap is limited and may not change the properties relevant to the conductance of the enzyme.
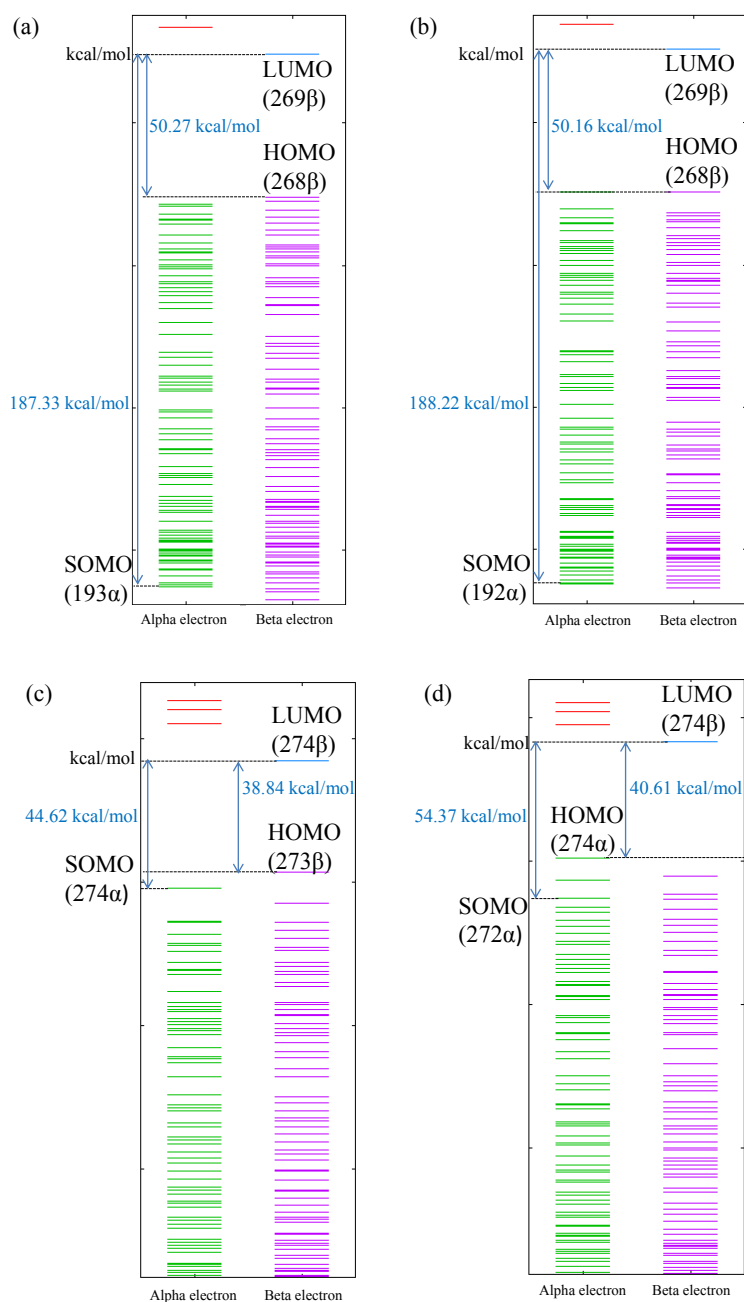
Figure 2.9. Energy profiles of the frontier orbitals of Models 1 and 2. In Model 1, energy differences between the SOMO and LUMO in (a) BS12 and (b) BS13 are 196.59 kcal/mol and 188.23 kcal/mol, respectively. In Model 2, energy differences between the SOMO and LUMO in (c) BS12 and (d) BS34 are 44.62 kcal/mol and 54.37 kcal/mol, respectively. In this manner, the energy levels of the SOMOs in Model 2 increase in the comparison with those of Model 1, due to the involvement of the hydroxyl ion, resulting in being close to those of the HOMOs.

2-3-2-3 Identification of single occupied molecular orbitals (SOMOs)

To identify the SOMOs of Models 1 and 2, we defined the following value D_j, which represents the difference in the contributions of the atomic orbitals between the LUMO and the j th occupied MO:

$$D_j = \sum_{i}^{N} (|C_i^{\text{LUMO}}| - |C_i^{j}|)^2 \ .$$

C_i^{LUMO} and C_i^{j} represent the coefficients of the i th atomic orbital in the LUMO and the j th occupied MO, respectively, and N is the number of the basis set. To identify the SOMOs, we quantitatively found the candidates of the SOMOs as the occupied MOs that exhibited the lowest D_j (thereby, we circumvented the ambiguity in the definition of a SOMO).

The analysis showed that the features of the SOMOs were actually similar to those of the LUMOs in Models 1 and 2 (Figure 2.10). However, the energy levels of the SOMOs were considerably different in Models 1 and 2, which means that the attachment of the hydroxyl ion dramatically increased the energy levels of the SOMOs in Model 2 (Figure 2.10).
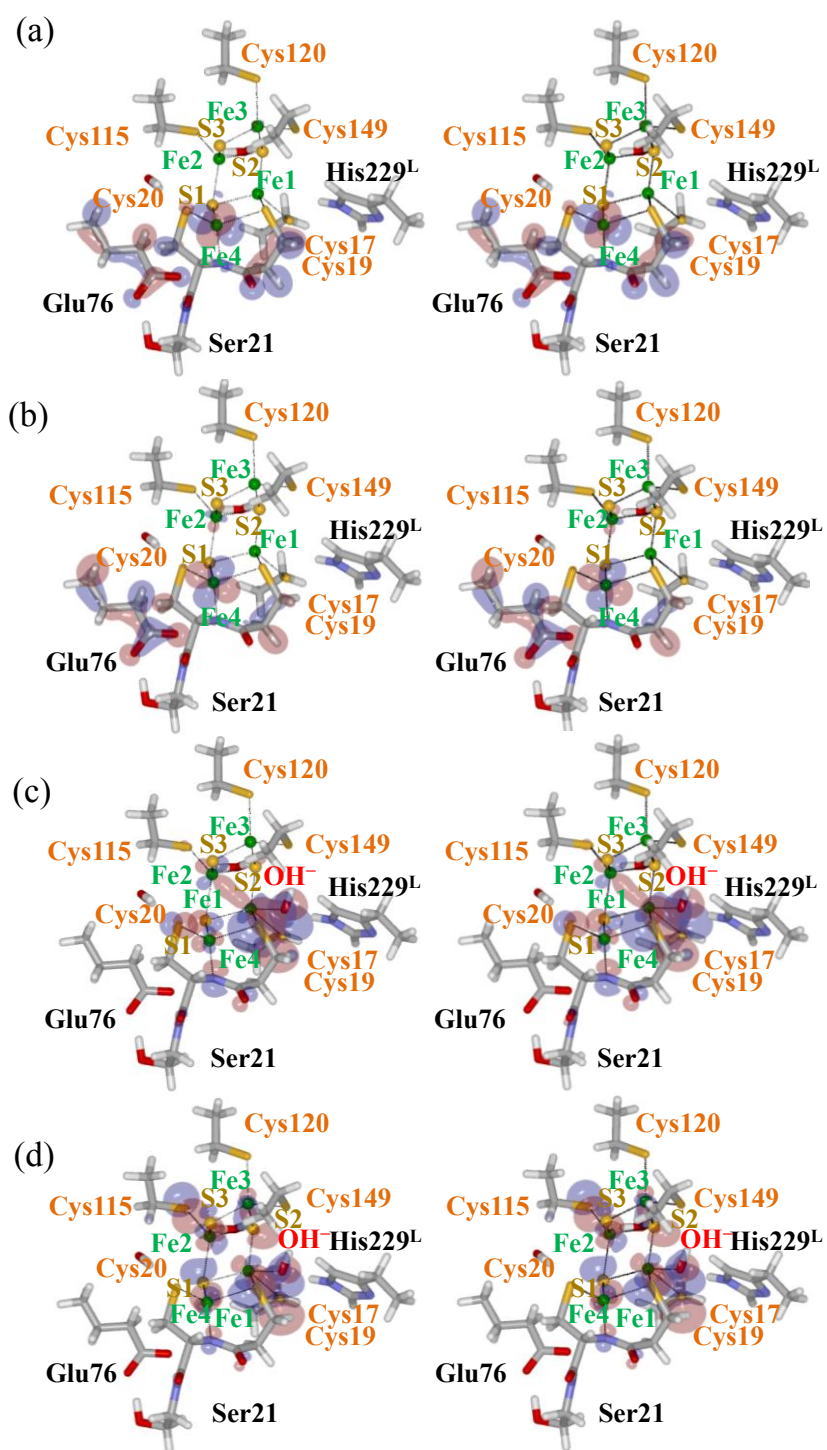
Figure 2.10. The SOMOs of Model 1 in BS12 (a) and BS13 (b), and those of Model 2 in BS12 (c) and in BS34 (d). The contour level to render the orbitals is 0.015

2-3-2-4 Hybridization aspects constituting LUMO and SOMO through attachment of hydroxyl ion

Motivated by the analysis to find the reason why the LUMO and SOMO in Model 2 were delocalized, we analyzed the MOs of Model 1 that would constitute the LUMO and SOMO in Model 2. As a result of the analysis, it was found that for both α and β electrons, the $3d$ orbitals of Fe4 and the $3p$ orbitals of S_{Cys19} and S_{Cys20} were hybridized, which generated the antibonding, nonbonding, and bonding orbitals in Model 1 (Figure 2.11). For example, for the β electrons in Model 1, the nonbonding and bonding orbitals that were generated by the hybridization correspond to MO258(β) and MO242(β), respectively (Figure 2.11b), and for the α electrons, the generated antibonding orbital was MO248(α) (Figure 2.11a).

In Model 2, the attachment of the OH$^-$ ion induced further hybridization with respect to the aforementioned generated orbitals in Model 1, $3p$ of S_{Cys17}, and $2p$ of the OH$^-$ itself, which also generated the antibonding, nonbonding, and bonding orbitals (Model 2). For example, for β electrons, the bonding MO242(β) (Model 1), $3p$ of S_{Cys17} (Model 1), and $2p$ of the hydroxyl ion were hybridized, which thus generated the antibonding [MO274(β)], nonbonding (unidentified), and bonding orbitals [MO237(β)] in Model 2 (Figure 2.11b). In this manner, the LUMO in Model 2, i.e., the antibonding MO274(β), was formed. For α electrons, $3p$ of S_{Cys17} (Model 1), the nonbonding MO258(α) (Model 1), the antibonding MO248(α) (Model 1), and $2p$ of the hydroxyl ion were hybridized, which thus generated the antibonding [MO274(α)], nonbonding, and bonding orbitals in Model 2 (Figure 2.11a). In this manner, the SOMO, i.e., the anti-bonding orbital MO274(α), was formed.

Next, in order to elucidate more detailed aspects of the changes in the major

components constituting the LUMO in Model 2, we analyzed the differences in the contributions of the basis set functions to the MOs of Model 2 in comparison with those of Model 1. As shown in Figure 2.11c, for both the LUMO of Model 2 and MO242(β) in Model 1, similar trends of the $C_i^{j\,2}$ values were found for the valence orbitals of S_{Cys17}, S_{Cys19}, S_{Cys20}, and Fe4, as follows. In the LUMO of Model 2 and MO242(β) of Model 1, four $3p$ and three $3d$ basis set functions were the main components describing these S and Fe atoms, respectively. For example, for S_{Cys17}, it was found that the contributions of the valence orbitals were in the order $3p_x > 3p_y > 3p_z$ in both the LUMO of Model 2 and MO242(β) of Model 1 (Figure 2.11c). Similarly, for S_{Cys19}, the contributions of the valence orbitals were found to satisfy $3p_z > 3p_x > 3p_y$ in both the LUMO of Model 2 and MO242(β) of Model 1. For S_{Cys20}, the contributions of the valence orbitals again satisfied $3p_z > 3p_x > 3p_y$ in both these MOs. For Fe4, the contributions of the valence orbitals satisfied $3d_{z2} > 3d_{x2-y2} > 3d_{yz} > 3d_{xy} > 3d_{zx}$ in both MOs (Figure 2.11c).

Accordingly, we concluded that MO242(β) in Model 1 was the main component in the LUMO of Model 2. On the other hand, in these two MOs, different features were also found. In the LUMO of Model 2, the $C_i^{LUMO\,2}$ values for the valence orbitals of Fe4, S_{Cys17}, and S_{Cys19} were larger than those of MO242(β) in Model 1, whereas those of S_{Cys20} were clearly smaller, even though to explain the systematic differences in the $C_i^{j\,2}$ values between the two MOs, the bias in the values was taken into account. This means that the attachment of the hydroxyl ion induced the changes in the orbital contributions through the hybridization (Figure 2.11c). As a consequence, the hydroxyl ion also changed the spatial distributions of these MOs and the energy levels, and thus

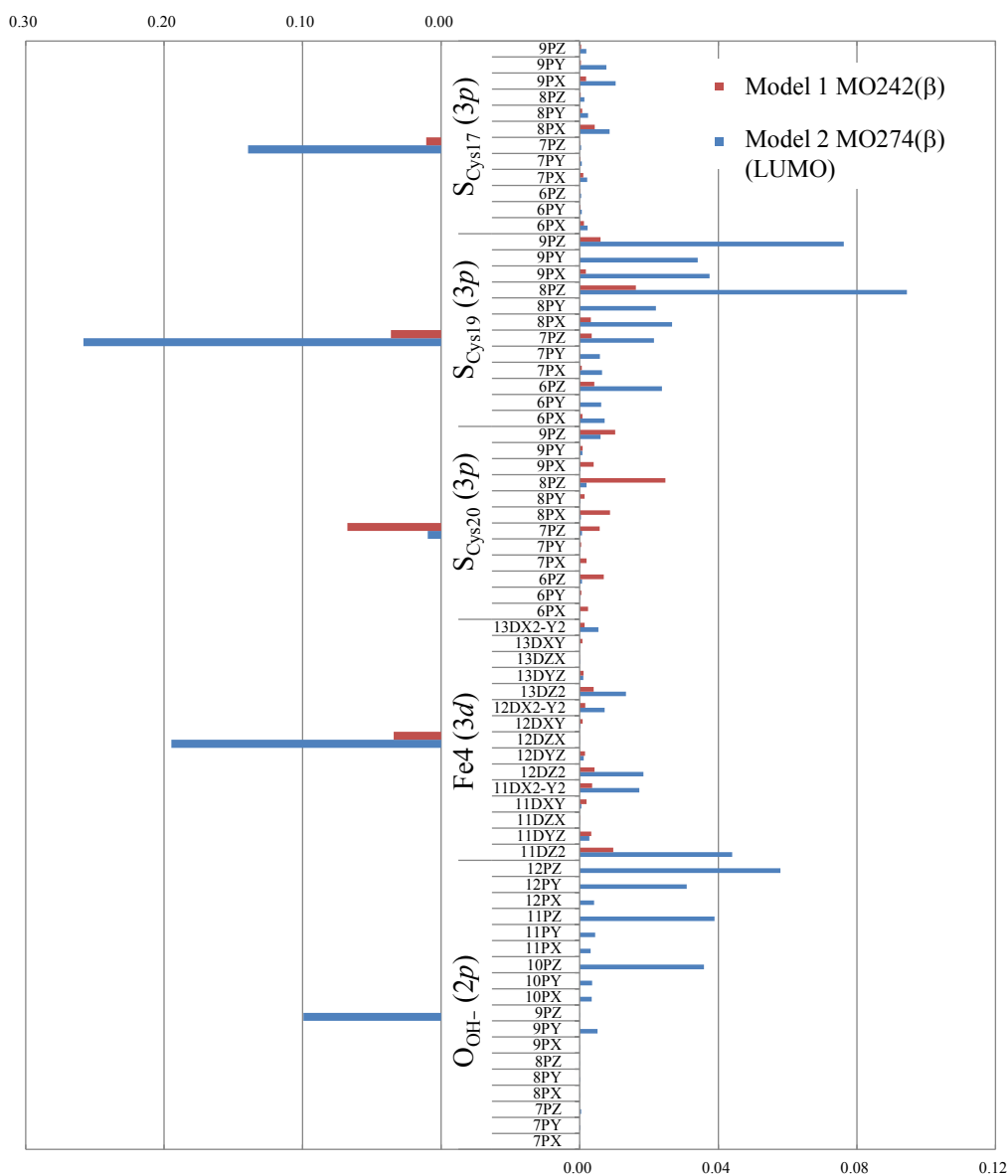created a delocalized LUMO (this is discussed further in the next section).

(a)

(b)
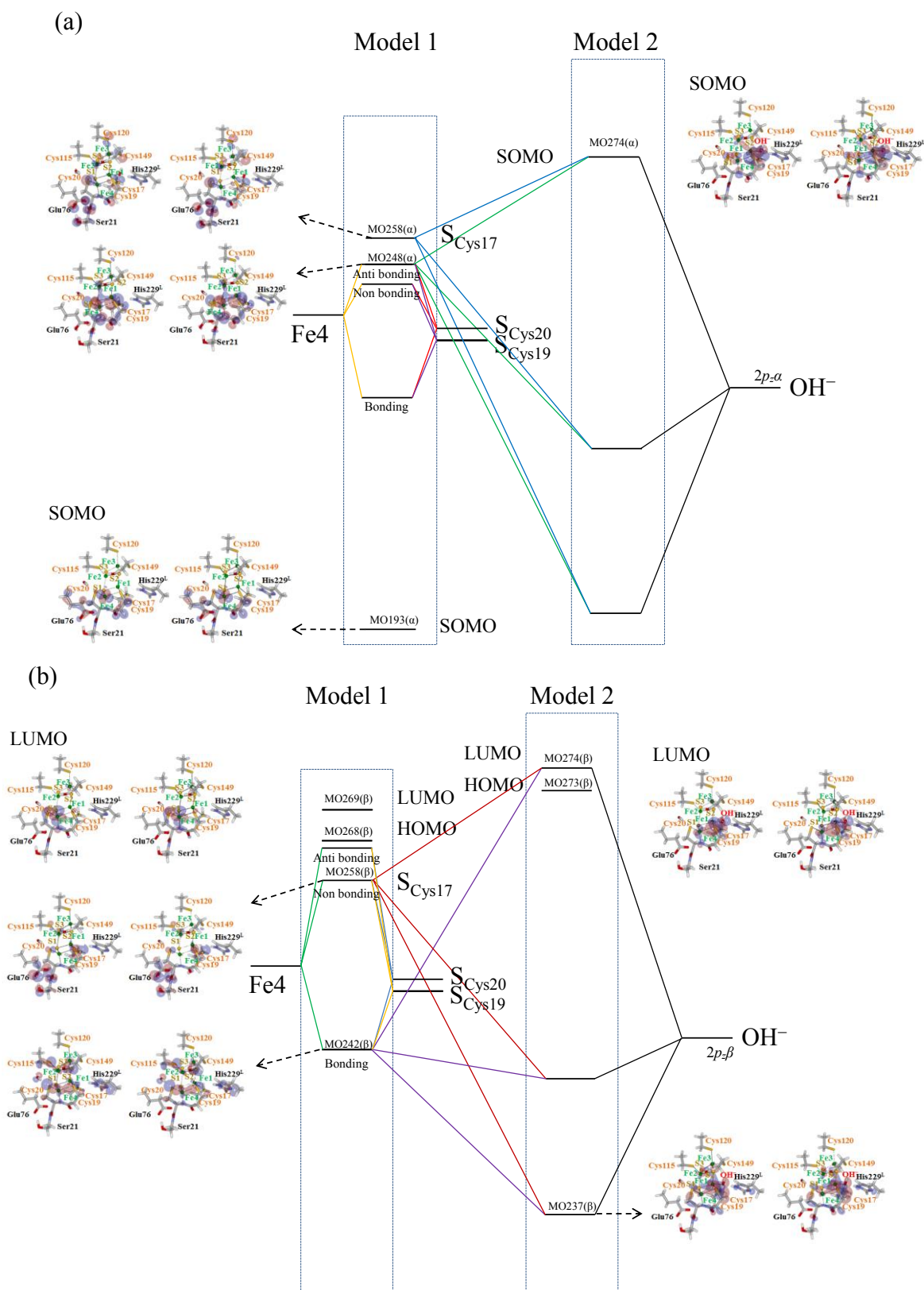
(c)

Figure 2.11. Hybridization aspects composing the LUMOs and SOMOs in Model 2 with stereo views of some relevant MOs, and quantitative analyses of the constitutive processes of the LUMO through comparison of Models 1 and 2. (a) Hybridization diagram of α electrons. The SOMO in Model 2 is an anti-bonding orbital that is constituted by hybridization of S_{Cys17}, MO248(α) that is an anti-bonding orbital made by Fe4, S_{Cys19}, and S_{Cys20} in Model 1, and the hydroxyl ion (for details, see section 2-3-2-4 in text). (b) Hybridization diagram of β electrons. The LUMO in Model 2 is an

anti-bonding orbital that is constituted by hybridization of S_{Cys17}, MO242(β) that is a bonding orbital made by Fe4, S_{Cys19}, and S_{Cys20} in Model 1, and the hydroxyl ion (for details, see section 2-3-2-4 in text). (c) Comparison of $C_i^{j\,2}$ values of the valence orbitals in MO242(β) of Model 1 and the LUMO of Model 2 (right plot), and the sums of those values in terms of each atom (left plot). These plots show that the LUMO in Model 2 and MO242(β) in Model 1 are similar, while differences in the two MOs are also found on S_{Cys17} and S_{Cys20} (for details, see section 2-3-2-5 in text).

2-3-2-5 Modulation of electron-delocalized spatial fields in LUMO and SOMO depending on attachment of hydroxyl ion

The present orbital analysis successfully provided the mechanisms that modulate the spatial distributions of the LUMO and SOMO through the attachment of the hydroxyl ion, as follows. Model 1 (lacking the hydroxyl ion) showed that Fe4 ($3d$) formed two covalent bonds, each with S_{Cys19} ($3p$) and S_{Cys20} ($3p$), thus intermediating the electron delocalization, which formed the S_{Cys19}-Fe4-S_{Cys20} segment as an electron-delocalized spatial field (also see Figure 2.1c). M Model 2 showed that the attachment of the hydroxyl ion induced the involvement of S_{Cys17} ($3p$) through the hybridization with the aforementioned $\underline{S_{Cys19}\text{-Fe4}}$-$S_{Cys20}$ segmental electronic field, whereas the contribution of S_{Cys20} decreased in the newly formed S_{Cys17}-HO$^-$-$\underline{S_{Cys19}\text{-Fe4}}$ electronic field (also see Figure 2.1c). Nevertheless, the hydroxyl ion preserved the electron delocalization in the new S_{Cys17}-HO$^-$-$\underline{S_{Cys19}\text{-Fe4}}$ spatial segment by intermediating between S_{Cys17} and the $\underline{S_{Cys19}\text{-Fe4}}$-$S_{Cys20}$ segment, which thus formed the new S_{Cys17}-HO$^-$-$\underline{S_{Cys19}\text{-Fe4}}$ segment as an electron-delocalized spatial field.

Although the HO⁻ forms a covalent bond with Fe1, the newly-formed electron-delocalized field marginally involves Fe1. Instead, this segmental electronic field, represented by the S_{Cys17}-HO⁻-S_{Cys19} moiety, is spatially formed by a non-bonded property relevant to the valence orbitals of the hydroxyl ion and the two sulfur atoms (S_{Cys17} and S_{Cys19}). Thus, a role of the HO⁻ in the electronic structure is to spatially bridge S_{Cys17} and the S_{Cys19}-Fe4-S_{Cys20} segmental electronic field (observed in Model 1) with the non-bonded property, and thereby creates the S_{Cys17}-HO⁻-S_{Cys19}-Fe4 segmental electronic field by eliminating the contribution of S_{Cys20}. Note here that the attachment of the hydroxyl ion also changed the energy levels of the MOs including the segmental electronic field, so as to create the reactive LUMO that was closely related to the ET (pathways) in the enzyme, as discuss for the regulation of the ET pathways below (see sect. **2-3.3** and **2-3.4**).

2-3-2-6 Spin density distributions

To obtain the spin density distribution, which is defined as $\rho_\alpha - \rho_\beta$, where ρ_α and ρ_β represent the electron densities of α and β electrons, respectively, we defined the spin densities of α and β electrons as follows:

$$\rho_A(\vec{r}) = \sum_{i}^{N_A} \left| \phi_i(\vec{r}) \right|^2 ,$$

where A is α or β, and N_A and ϕ_i represent the total number of α or β electrons and the i th MO, respectively.

In Model 1, the major spin density distributions were found on the four Fe ions in both the BS12 and BS13 spin states (Figure 2.12a, b). By contrast, in Model 2, the spin density distributions were observed on the O atom of the hydroxyl ion and on S_{Cys19} as

well as the four Fe in both BS12 and BS34 (Figure 2.12c, d). Thus, the SOMOs were more delocalized than the spin density distributions in both Models 1 and 2, while the spin densities were almost localized on the four Fe ions (Figure 2.12).

This difference between the SOMOs and the spin density distributions may be derived from the different shapes of the corresponding MOs of α and β electrons caused by complicated interactions of orbitals and the distinct numbers of α and β electrons. More specifically, the total spin of the entire system is 1/2, and so the SOMOs can be represented by one electron in the simplest, ideal case. However, SOMOs and spin density distributions are not necessarily identical. Moreover, since the present systems include the distinct spin states of Fe ions (Table 2.3) and the complicated, distorted configurations in the [4Fe-3S] cluster (Figure 2.1c), differences between the SOMOs and spin densities are enhanced. Despite these differences between the SOMOs and the spin density distributions, both distributions commonly included the O atom of the hydroxyl ion in Model 2 (Figure 2.10c, d and Figure 2.12c, d).

In this manner, the hydroxyl ion affected the SOMOs and the spin density distributions as well as the frontier orbitals, and these findings may be relevant to the ET pathways and mechanisms, although to elucidate such detailed aspects, further analyses of the electronic structures are required in the near future.
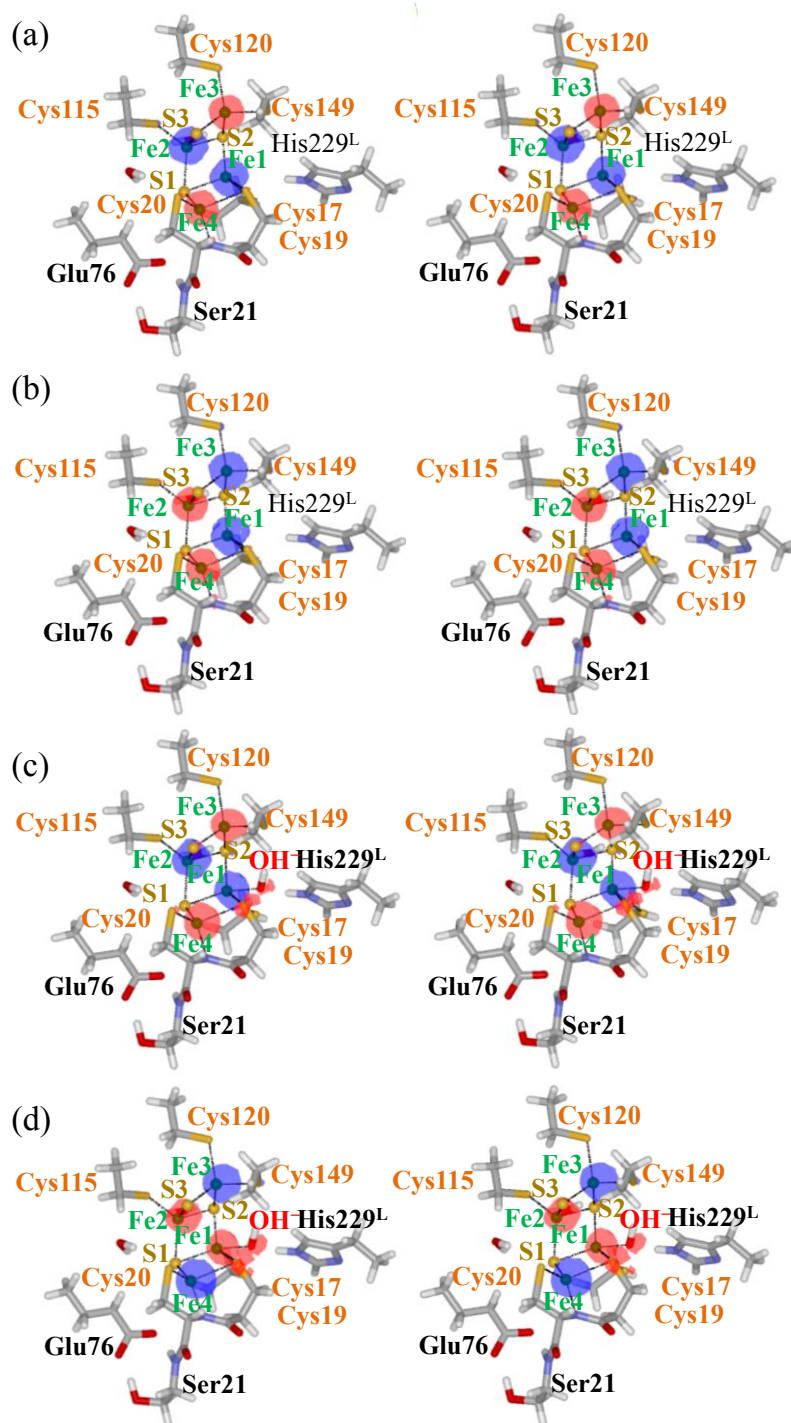
Figure 2.12. Spin density of Models 1 and 2. Red and blue contours show plus and minus spin states, respectively. In Model 1 ((a) BS12 and (b) BS13), the spin density distributions are observed only on Fe ions. In contrast, in Model 2 ((c) BS12 and (d) BS34), the spin densities are also distributed on S_{Cys19} and O atom of the hydroxyl ion.

2-3-2-7 Effects of amino acid residues in the peripheral of core cluster

Next, in order to analyze the effects of Ser21, Glu76, His229, and two crystal water molecules in the proximal cluster on the electronic properties of Models 1 and 2, we removed these structural moieties from Models 1 and 2 (referred to here as Models 3 and 4, respectively), and performed *ab initio* electronic structure calculations of Models 3 and 4. The most favorable spin assignments were explored and identified to be BS12 and BS13 for Model 3 and BS12 and BS34 for Model 4. This result is identical to that for Models 1 and 2, respectively. The analysis of the obtained electronic structures showed that the frontier orbitals of Models 3 and 4 were almost identical to those of Models 1 and 2, respectively (data not shown). Thus, we concluded that in Models 1 and 2, the frontier orbitals of the [4Fe-3S] cluster in the super-oxidized state were marginally affected by Ser21, Glu76, His229, and the two crystal water molecules.

2-3-3 ET pathways

In the mechanisms that have been proposed to date to explain the O_2 tolerance of MBHs, the ET processes through the four functional clusters are involved, as discussed below (also see the next section). In this study, to investigate the ET pathways between the proximal cluster and the [NiFe] active site, we employed an empirical method using the *pathway* plugin of VMD.[36)] In the ET pathways with the highest T_{DA} value, which were identified as routes from Ni in the [NiFe] active site to Fe ions of the proximal cluster, the following atoms were found to be commonly involved; S_{Cys75L}, βC_{Cys75L}, αC_{Cys75L}, C_{Cys75L}, N_{Gly76L}, O_{Cys17}, C_{Cys17}, αC_{Cys17}, βC_{Cys17}, S_{Cys17}, and Fe1 (Figure 2.13). Similarly, we also investigated the ET pathways between the medial and proximal clusters. The identified pathways commonly passed through Fe4 in the medial cluster,

S_{Cys252} (the medial cluster), the hydrogen bond between S_{Cys252} and the amide proton of the Cys149 backbone (the proximal cluster), α and β carbons of Cys149, S_{Cys149}, and Fe3 in the proximal cluster (Figure 2.13).

The obtained results led us to the following idea regarding the ET pathways through the [NiFe] active site, the proximal cluster, and the medial cluster, by combining the results of the electronic structure analysis conducted in the present study. The delocalized LUMO of Model 2 is sandwiched by the [NiFe] active site and the SOMO (Figure 2.13 and 2.10), since the latter MO is more delocalized in the proximal cluster. Thus, the pathway composed of the delocalized LUMO can transfer a single electron from the [NiFe] active site to the central core moiety of the proximal cluster. In fact, the ET pathway that was identified by the empirical method closely overlaps with the delocalized LUMO of the proximal cluster. In this manner, the hydroxyl ion may create an ET pathway through delocalization of the LUMO in the proximal cluster, thus driving the reaction cycle of the O_2-tolerant MBHs (as discussed below).

The proximal cluster of MBHs exhibits three distinct redox states, i.e., the super-oxidized ([4Fe-3S]$^{5+}$), oxidized ([4Fe-3S]$^{4+}$), and reduced states ([4Fe-3S]$^{3+}$),[28] and two types of structural forms are changed in the proximal cluster, depending on these redox states (Figure 2.1c and Figure 2.2).[21] One structural form, which is referred to here as "Strc2" (Table S4), is observed in the super-oxidized state, and the other structural form, which is referred to here as "Strc1", is observed in the reduced states (Figure 2.2). Although for the oxidized state, the structural feature of the proximal cluster has not been clarified unambiguously, a previous study[21] suggested that the Strc1 form appeared upon chemical treatment, which may provide a single electron to the super-oxidized proximal cluster.
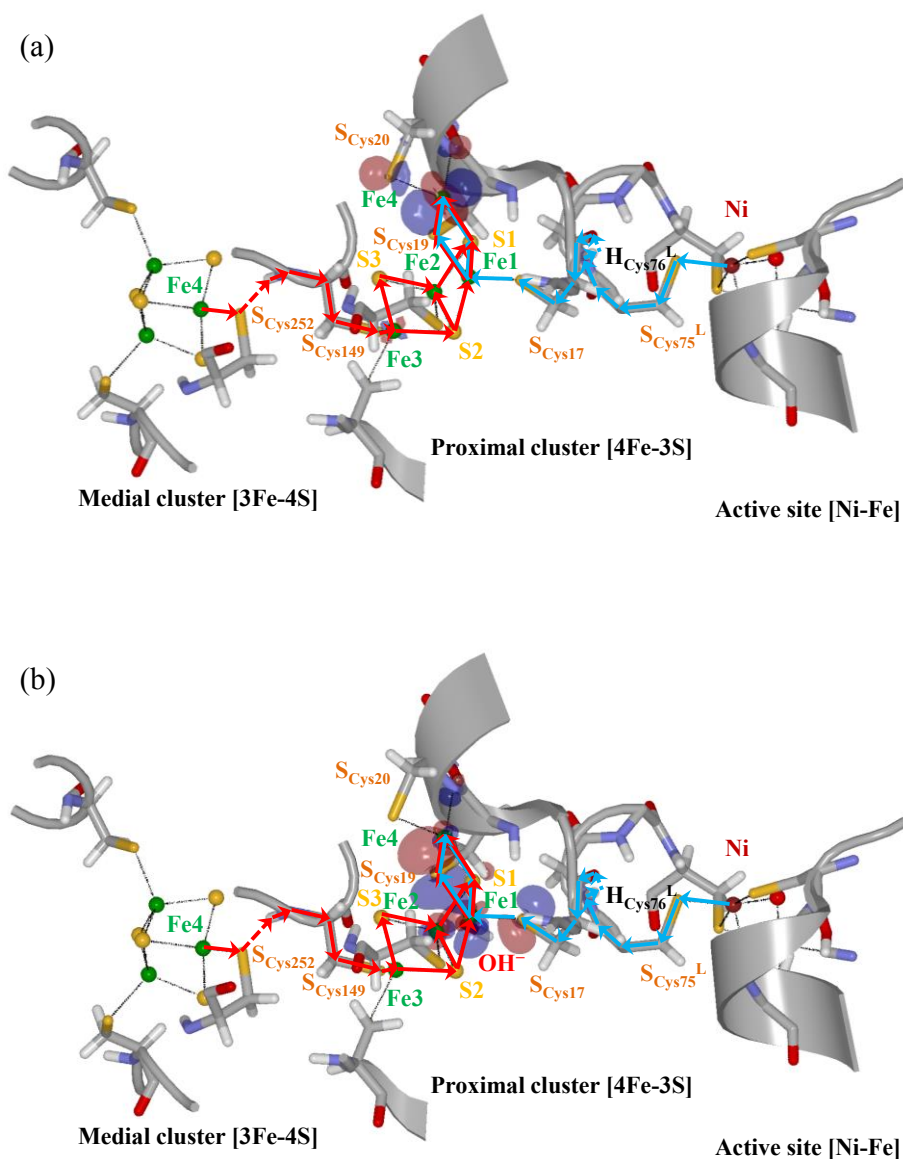
Figure 2.13. The plausible ET pathways obtained employing an empirical method (*pathway*) to search for the ET pathways. The blue line with an arrow (pathway A) shows the ET pathway from the [NiFe] active site to the proximal cluster, and the red line with an arrow (pathway B) shows the ET pathway from the medial to proximal clusters. Both ET pathways pass through the localized and delocalized LUMOs identified in Model 1 (a) and Model 2 (b), respectively. As a result, these LUMOs in Models 1 and 2 are marginally and significantly overlapped, respectively, with the above-mentioned ET pathways.

This invokes the idea that the structural change from Strc2 (the super-oxidized state) to Strc1 (the oxidized state) is a trigger induced by the ET of MBHs in the reactivation process as follows. Radu et al. recently suggested that the super-oxidized state of the proximal cluster interrupts the functioning of the iron-sulfur electron relay (Table 2.5).[44] To recover the iron-sulfur electron relay, the attachment of the hydroxyl ion to the proximal cluster would promote the above-mentioned structural change in the proximal cluster as a functional trigger induced by the ET that is controlled by the redox state of the [NiFe] active site. Thus, the ET mechanism proposed in the present study could induce the single-electron reduction of the super-oxidized state, resulting in the recovery from the resting state of the iron-sulfur electron relay (Table 2.5).

Redox state		Structure	FeS relay
Super-oxidized	$[4Fe\text{-}3S]^{5+}$	Strc2	No
Oxidized	$[4Fe\text{-}3S]^{4+}$	Strc1	Yes
Reduced	$[4Fe\text{-}3S]^{3+}$	Strc1	Yes

Table 2.5. The relationships between the structure and functioning in the FeS electron relay, depending on the redox state. Strc1 (Figure 2.2) and Strc2 (Figure 2.1c) represent the geometries in the reduced and super-oxidized state.

In previous studies, the redox potentials upon the reduced/oxidized and oxidized/super-oxidized transitions were measured; -60 and $+160$ mV for *Ralstonia*

eutropha MBH,[44] and +98 and +232 mV for *Aquifex aeolicus* hydrogenase 1 (AaHyd-1), respectively.[23] Similarly, for *Escherichia coli* hydrogenase 1, the small potential difference of less than 220 mM between the two redox couples was observed.[45] Such narrow potential gaps between the two redox pairs in the proximal clusters of these O_2-tolerant hydrogenases allow the second oxidation to occur.[46] The effects of the OH^- ion should also be analyzed theoretically in terms of the redox potentials in the near future, in combination with the electronic structure that were elucidated in the present analysis (also see the discussion below).

In summary, the attachment of the hydroxyl ion induces the delocalization of the LUMOs, and thus forms a bridge between the proximal cluster and the [NiFe] active site, which create the ET pathway between these two functional cluster sites. This should be further examined by estimating the relevant factors such as the reorganization energy[47] in the electron transfer rates, k_{ET} (see section 2-2-5), which is an on-going study in our group involving the use of hybrid *ab initio* quantum mechanics/molecular mechanics (QM/MM) calculations of the entire enzyme with the explicit inclusion of the solvent water molecules. In the next section, we further discuss more comprehensive roles of the hydroxyl ion in the catalytic reaction cycle of MBHs.

2-3-4 Role of OH^- in the O_2-tolerance of MBHs

In the presence of O_2, the catalytic activities of MBHs are lowered (but are still sustained at the reduced levels), and the [NiFe] active site is changed to the inactive state, i.e., the Ni-B state:[48] O_2 attack induces the Ni-B state through the four-electron reduction. If one assumes that all the FeS clusters of MBHs are reduced prior to the O_2 attack, the proximal cluster, the medial cluster, and the [NiFe] active site provide two,

one, and one electron, respectively, to reduce O_2, although the distal cluster remains to be reduced.[49] Here, to recover the catalytic activity of MBHs from the inactivated state, the [NiFe] active site must be changed to the Ni-SI state (Figure 2.14).[48]

To explain this mechanism, two recovery processes occurring on the [NiFe] active site have been proposed: First, Volbeda et al.[50] suggested that the reactivation of MBHs can be enhanced by the formation of an MBH dimer. More specifically, in the MBH dimer, an inactivated MBH molecule can be reduced by the other activated MBH molecule in the dimer. Thus, at least two electrons are transferred between the two distal clusters of the MBHs in the dimer.[50] Second, Kurkin et al.[51] suggested that the reactivation mechanism is initiated from the reduction of the [NiFe] active site in the presence of H_2, which should activate the inactive MBH, although the process requires a few seconds (note here that the O_2-sensitive hydrogenases such as the standard [NiFe] hydrogenase require over 1 h to be reactivated).[51] [51] In this process, H_2 cleavage occurs, which changes the Ni-B state of the [NiFe] active site into the Ni-SI state, and thus four electrons are evolved from these two states, thereby reducing the proximal and medial clusters. This process further induces the structural change from Strc2 to Strc1 in the proximal cluster.[51] Notably, this is the opposite ET direction to that in the mechanism proposed by Volbeda et al.

In the present analysis, we indicated that the attachment of the hydroxyl ion induces the delocalization of the LUMO in the proximal cluster; i.e., in Model 2, the LUMO is delocalized on S_{Cys17}, S_{Cys19}, and Fe ions of the proximal cluster (see section 2-3-2-1). For the ET from the [NiFe] active site to the proximal cluster, the pathways, identified by the empirical method, commonly pass through a hydrogen bond between the O atom of the Cys17 backbone (O_{Cys17}) and the N atom of the Gly17^L backbone

(located in the large subunit) (N_{Gly76L}) (for more details, see section 2-3-3). This possible ET pathway significantly overlaps with the delocalized LUMOs that were identified in the proximal cluster of Model 2, and thus the productive ET pathway might be generated by the attachment of the hydroxyl ion to Fe1 in the proximal cluster (Figure 2.13). In this manner, we concluded that the attachment of the hydroxyl ion may critically contribute to the ET in both mechanisms (i.e., the ET from the [NiFe] active site to the proximal cluster, and from the distal to proximal clusters).

More specifically, we further conjecture the ET mechanism, which could be promoted by the attachment of the hydroxyl ion in the proximal cluster, to be as follows. A conserved glutamate (Glu) residue, Glu76, which is located close to the proximal cluster (Figure. 2.1), exhibits two types of distinct conformational features that have been found in *Hydrogenovibrio marinus* and *Escherichia coli* MBHs. Note here that in *Ralstonia eutropha* MBH, where the hydroxyl ion has been identified, Glu76 exhibits only a stable conformation in the crystal structure (this structure corresponds to Strc2) (see Figure 2.1c. 1c and Table 2.4), which is equivalent to one of the two conformations observed in the other two systems (another structure is referred to here as Strc3). In Strc3, which is equivalent to one of the two conformations observed in the other two systems (the other structure is referred to here as Strc3). In Strc3, which is more favorable in energy by 2−5 kcal/mol than the other structure (Strc2), the Fe4-O^{ε}_{Glu76} bond is formed, but the Fe4-S_{Cys19} covalent bond is lost (note here that the energy evaluation was performed in terms of the structure without the hydroxyl ions).[42]

Moreover, in a previous study, it was proposed that the acceptance of a single electron in Strc2 may enhance the conformational change from Strc2 (super-oxidized state) to Strc1 (oxidized state) (see Figure 2.2 and Table 2.4).[21] We can infer (from the

"hardness" of the atoms) that in Strc2, the N_{Cys20} atom could provide an electron to the central core moiety of the proximal cluster through the Fe4-N_{Cys20} bond. Furthermore, in the present study, we showed that the attachment of the hydroxyl ion creates ET pathways in the proximal cluster by generating the S_{Cys17}-$\underline{HO^-}$-S_{Cys19}-Fe4 segmental electronic field, which is a main component of the delocalized LUMO (see sect. **2-3.2.5**), thus promoting the ET.

On the basis of these data, we propose that the attachment of the hydroxyl ion may promote the reaction stage corresponding to the above-mentioned ET, by which the conformational change from Strc2 to Strc1 would be induced. Actually, in Strc1, the Fe4-N_{Cys20} bond is lost, and thereby the electron is not provided from N_{Cys20} to the central core moiety of the proximal cluster, which is reasonable after the acceptance of one electron. Thus, the hydroxyl ion may induce this stage involving the ET toward the proximal cluster from either the [NiFe] active site or the medial cluster (Figure 2.13), [50,51] which further leads to the structural change from Strc2 to Strc1, in the O_2-tolerant catalytic cycle of MBHs (see Refs. 10 and 46).

On the other hand, in Strc3, Glu76 forms a covalent bond with Fe4, and thus the ET mechanism could be different from that in Strc2 mentioned above. To reveal the role of the Glu residue and the functional relationship between the Fe4-O^{ε}_{Glu76} bond formation (found in *Hydrogenovibrio marinus* and *Escherichia coli* MBHs) and the attachment of the hydroxyl ion (*Ralstonia eutropha* MBH), further detailed analyses are necessary.
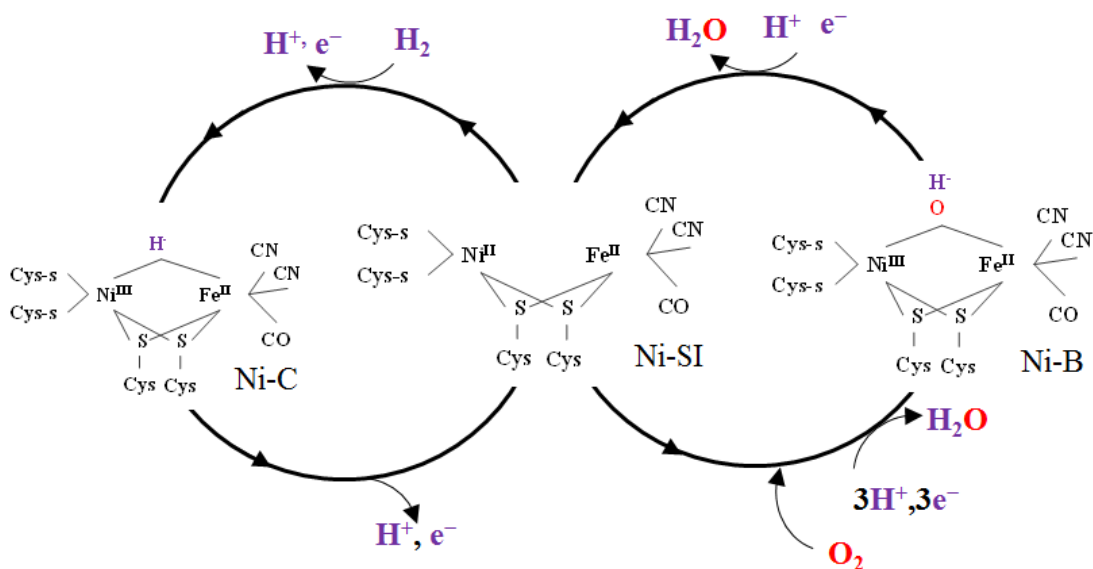
Figure 2.14. The Ni atom in the [Ni-Fe] active site is coordinated by four Cys residues, two of which bridge Fe^{2+}. Ligands bridging the Ni and Fe atoms are hydride and hydroxyl ion in the Ni-C and Ni-B states, respectively. In the presence of O_2, O_2 is rapidly reduced by four electrons provided by the ET relay, and then one of the oxygen atoms is reduced to H_2O. This reaction forms the Ni-B sate. Provided that one electron and proton are supplied, the hydroxyl ion bridging the Ni and Fe ions is reduced to H_2O. Then, the [NiFe] active site re-establishes the catalysis of H_2.[46]

2-3-5 Perspectives

From a technical viewpoint, the present *ab initio* calculations employing the B3LYP functional should be evaluated by employing more advanced QM methodologies in the near future, although this functional has been shown to work for an extremely broad range of materials. In fact, for the [NiFe] active site, it was reported that the B3LYP functional significantly underestimated the total energy values,[52] while for the proximal cluster, the B3LYP functional reportedly worked well.[21,42] Furthermore, the orbital

analysis performed in the present study should be further examined by employing the reconstituted orthogonal orbitals, such as the Wannier function,[53,54] which is also an ongoing study by our group.

Among the crystallographic data of MBHs, some amino acid residues around the proximal cluster exhibit multiple conformations, for which the significance is still unknown. To resolve this, geometrical and electronic structure analyses employing hybrid *ab initio* QM/MM calculations coupled with long-time-scale molecular dynamics (MD) simulations are required, thereby enabling us to clarify the detailed energetics and functional roles that are relevant to these multiple conformations. This methodology also enables us to theoretically estimate the electron transfer rates and the relevant redox potentials (see sect. **2-3.3**). Furthermore, the electronic structure analyses of larger structures where more than two transition-metal binding clusters are involved, such as the medial and proximal clusters, would elucidate the "communications" of the functional clusters in the reaction cycle of the enzyme. Such analyses are also ongoing by our group.

2-4. Conclusion

To investigate the functional roles of the hydroxyl ion (OH^-) that was experimentally identified in the proximal cluster of *Ralstonia eutropha* MBH, we conducted *ab initio* electronic structure calculations of the [4Fe-3S] proximal cluster, employing structural models with and without the hydroxyl ion attached to Fe1. The analysis revealed that the attachment of the hydroxyl ion changed the optimal spin assignments in the proximal cluster, which also induced the changes in the electronic structure. The most notable change induced by the hydroxyl ion is the induction of

significant rearrangements of the frontier orbitals. As a consequence, the LUMO was spatially delocalized and was thus distributed toward the [NiFe] active site through the formation of S_{Cys17}-$\underline{HO^-}$-S_{Cys19}-Fe4 segmental electronic field, which may bridge the ET from the [NiFe] active site in the large subunit to the proximal cluster in the small subunit.

In fact, an empirical method to search for the ET pathways identified plausible pathways that significantly overlapped with the aforementioned LUMO. Conversely, without the hydroxyl ion, the LUMO marginally overlapped with the ET pathways identified. In this manner, we indicated that the hydroxyl ion modulated the LUMO, thereby creating the ET pathways from the [NiFe] active site to the proximal cluster.

This delocalized LUMO of the proximal cluster in the presence of the hydroxyl ion was not distributed toward the medial cluster. However, the empirical method used to search for the ET pathways also identified the plausible ET pathways from the medial to proximal clusters that passed through the aforementioned LUMOs. As a result, the ET pathways from the medial to proximal clusters well overlapped with the S_{Cys17}-$\underline{HO^-}$-S_{Cys19}-Fe4 segmental electronic field in the LUMO of the proximal cluster (in the presence of the hydroxyl ion). Thus, we showed that the LUMO generated by the attachment of the hydroxyl ion also contributed to the ET from the medial to proximal clusters. By contrast, in the absence of the hydroxyl ion, the LUMO of the proximal cluster marginally overlapped with the ET pathways.

Accordingly, the attachment of the hydroxyl ion to Fe1 in the proximal cluster may create the productive ET pathways in both directions, i.e., the pathways from the [NiFe] active site to the proximal cluster and from the medial to proximal clusters. This promotion of the ETs should induce single-electron reduction of the super-oxidized

proximal cluster, which may cause the structural change from the super-oxidized (Strc2) to oxidized forms (Strc1). While the super-oxidized proximal cluster prevents the electron relay activity, the aforementioned structural change may reinvoke the electron relay. Thus, the proximal cluster acts as a "functional hub" that is controlled by the attachment of the hydroxyl ion to the ET pathways, as well as the changes in the redox state, in the O_2-tolerant catalytic cycle of the hydrogenases.

This is the first report of the orbital analysis of the proximal cluster of MBHs in the presence and absence of the hydroxyl ion. The obtained data and conclusions described above provide a solid basis for the future experimental and theoretical analyses of mechanisms of the O_2-tolerant catalytic reaction by the hydrogenases.

Chapter 3

Exploration of optimal spin assignments of [3Fe-4S] medial cluster of hydrogenase employing *ab initio* electronic structure calculation

3-1. Introduction

In the previous chapter, we identified the optimal spin states of the proximal cluster of *Ralstonia eutropha* membrane bound hydrogenase (MBH) in the super-oxidized state, employing *ab initio* electronic structure calculation.[55] It has been believed that the super-oxidized state of the proximal cluster plays an important role in the O_2-tolerant reaction cycle of the hydrogenases. Accordingly, to investigate its electronic structure, we explored the optimal spin state of the proximal cluster in the super-oxidized state in Chapter 2. Notably, we performed this analysis using the structural models in the presence and absence of hydroxyl ion (OH^-) that was experimentally revealed to be attached to an iron (Fe) ion in the central core moiety of the proximal [4Fe-3S] cluster.

In this chapter, for the medial cluster in the reduced and oxidized states, we explored optimal spin states, since the medial cluster was found to exhibit these two redox states in the catalytic cycle of MBHs. The transition from the reduced state to the oxidized state could transfer an electron from the medial to proximal clusters, the latter of which could be in the super-oxidized.[48] If the medial cluster is reduced by the distal cluster, the medial cluster could intermediate the electron transfer (ET) from the distal cluster to

the proximal cluster and the [NiFe] active site (see Chapter 2).[55] This reaction process would activate inactive hydrogenases. To reveal the mechanism of the ET from the medial cluster to the proximal cluster, it is required to investigate the electronic structure of the structure involving the proximal and medial clusters as well as the isolated medial cluster. For this aim, we explored the optimal spin states of the medial cluster in this study.

Moreover, we investigated electronic structures of the fused models where the proximal and medial clusters were both involved, as those of the super-oxidized state and the reduced or oxidized states, respectively. Notably, in our previous study, we revealed that the hydroxyl ion attached to the proximal cluster induced the LUMO that were spatially delocalized toward the [NiFe] active site. This type of the LUMO was significantly overlapped with the electron transfer (ET) pathways that were theoretically identified in a manner independent upon the *ab initio* electronic structure calculations. Thus, the present analysis is expected to elucidate "communications" between the proximal and medial clusters, through comparison with each of those isolated functional clusters.

3-2 Computational Methods

3-2-1 Model Building

For *ab initio* quantum mechanics (QM) calculation, a structural model of the medial cluster, which is referred to here as Model(m), was constructed employing the atomic coordinates of *Ralstonia eutropha* MBH in a partially reduced state (PDB entry: 4IUD) (Figure 2.1). Model(m) harbores the [3Fe-4S] core moiety, Lys226, Asn228, Trp235, Ser253, peptide bond between Cys249 and Ile250 and three coordinated

cysteine (Cys) residues (i.e., Cys230, Cys249, and Cys252), which were truncated by replacing the C_α atoms with a methyl group (-CH$_3$) (Figure 3.1).

For the fused structure of the proximal and medial clusters, two types of models were constructed, and referred to here as Models(mp) 1 and 2: Model(mp) 1 consists of the proximal cluster in which the hydrogen atoms in the proximal cluster were optimized in BS12, and the medial cluster in which the hydrogen atoms were optimized by classical mechanics. Model(mp) 2 is composed of the proximal cluster in which the hydrogen atoms were optimized in BS34, and the medial cluster in which hydrogen atoms were optimized by classical mechanics.

Models(mp) 1 and 2 harbored the proximal and medial cluster parts. The proximal cluster part contained [4Fe-3S], and six Cys residues (i.e., Cys17, Cys19, Cys20, Cys120, Cys115, and Cys149) that coordinate to the Fe ions. Moreover, Ser21, Glu76, His229, two crystal water molecules that coordinate to [4Fe-3S], and three peptide bonds between Cys19 and Cys20, between Cys20 and Ser21, and between Gly148 and Cys149, were included. Four cysteine residues (i.e., Cys17, Cys115, Cys120, and Cys149), Glu76, and His229 were truncated by replacing the C_α atoms with a methyl group (-CH$_3$). The medial cluster parts harbored [3Fe-4S], and three coordinated cysteines (Cys) residues (i.e., Cys230, Cys249, and Cys252), which were truncated by replacing the C_α atoms with a methyl group (-CH$_3$). Moreover, Lys226, Asn228, Trp235, Ser253, and the peptide bond between Cys249 and Ile250 were included (Figure 3.2).
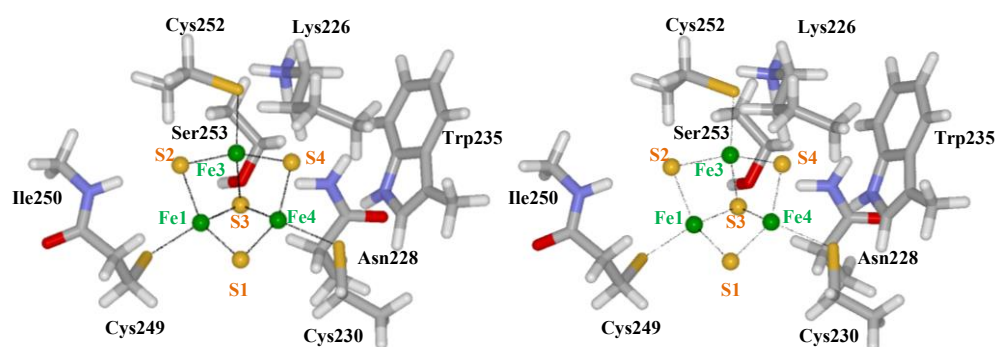
Figure 3.1. Stereo view of Model(m) including 95 atoms employed for our *ab initio* calculations of the medial cluster in the reduced and oxidized states. This structural model was extracted from the crystal structure of *Ralstonia eutropha* membrane bound hydrogenase (MBH) (PDB entry: 4IUD).
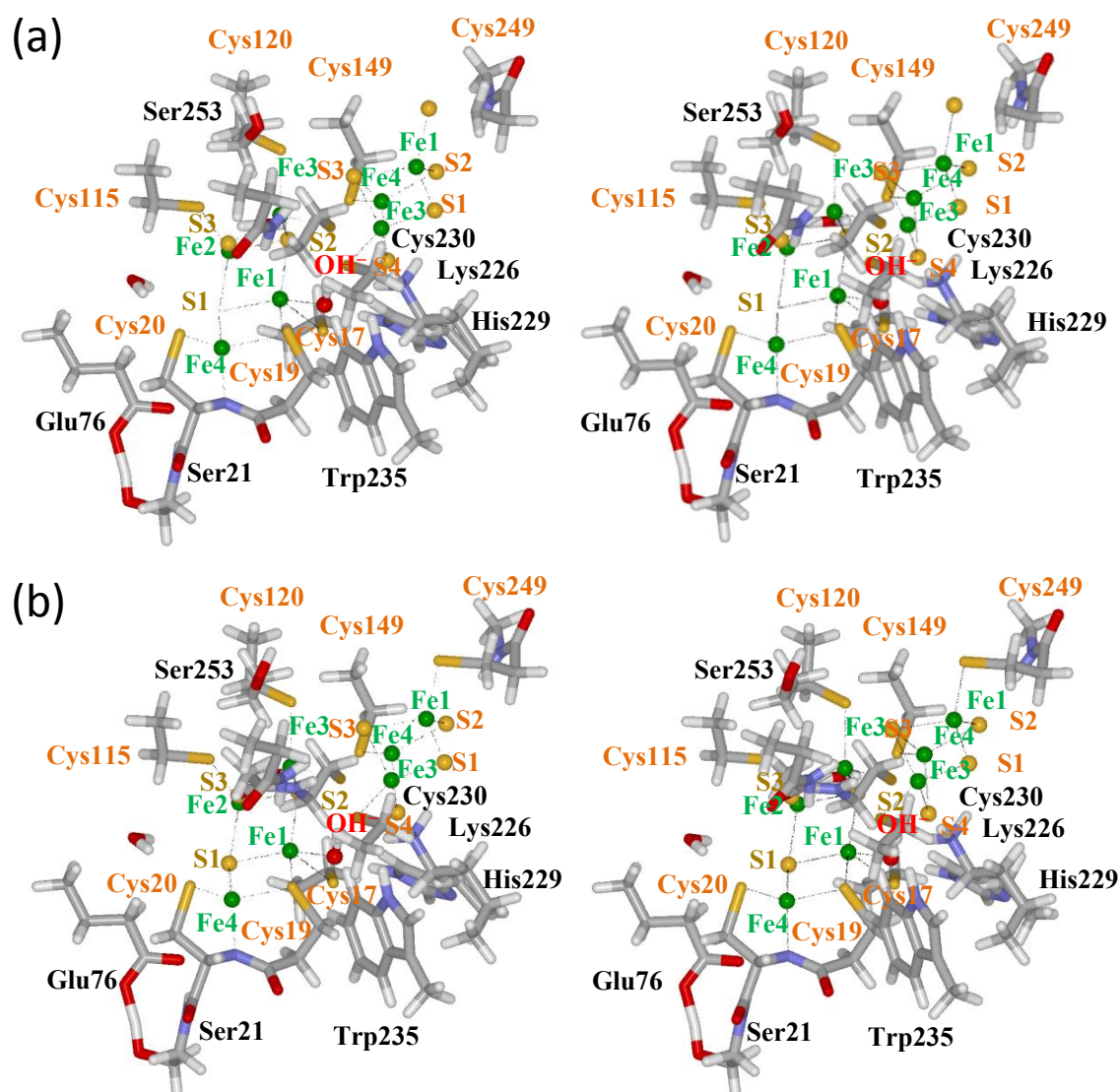
Figure 3.2. Stereo view of Models(mp) 1 and 2 including 205 atoms employed for our *ab initio* calculations of the fused strcuture of the proximal and medial clusters, with the distinct spin combinations (see text). The atomic coordinateds were extracted from the crystal structure of *Ralstonia eutropha* membrane bound hydrogenase (MBH) (PDB entry: 4IUD).

With respect to these structural regions extracted for the present analysis, the root mean square deviation (RMSD) between the H_2-reduced state (PDB entry: 3RGW) of *Ralstonia eutropha* MBH and the partially reduced state of *Ralstonia eutropha* MBH was as small as 0.067 Å. Moreover, the RMSD between the partially reduced state and the aerobically-oxidized state is also small (i.e., 0.0283 Å). Thus, Model(m) can also be employed as the oxidized and reduced charge states of the medial cluster.

3-2-2 Exploration of spin assignment of the Medial cluster

The [3Fe-4S] medial cluster is reportedly composed of Fe^{2+} or Fe^{3+}, and S^{2-}.[23,28] The formal charge of the [3Fe-4S] medial cluster was spectroscopically identified as 0 and +1 in the reduced and oxidized states, respectively. Accordingly, the core moiety is composed of four S^{2-}, two Fe^{3+}, and one Fe^{2+} in the reduced state, and, three Fe^{3+} and four S^{2-} in the oxidized state. In addition, the total spin of the [3Fe-4S] medial cluster was identified as 2 and 1/2 in the reduced and oxidized states, respectively.[23,28]

In terms of Fe^{2+} and Fe^{3+}, all the high, middle, and low spins were considered to construct the possible spin combinations, with 2 in the reduced state and 1/2 in the oxidized state as the total spin. To provide the spin assignments of the [3Fe-4S] medial cluster, the nomenclature [A, B, C] is employed here, where A, B, and C are corresponding to the multiplicities that are assigned to Fe1, Fe3, and Fe4, respectively (in this report, the residue numbering system is subjected to that of *Ralstonia eutropha* MBH).[21] In addition, α and β spins are specified employing the sign of multiplicities: For example, [−6, 5, 6] in the reduced state indicates that Fe1, Fe3, and Fe4 are

assigned to β spin of sextet, α spin of quintet, and α spin of sextet. Thus, the spin state

assigned to the iron ions is described as (Fe1, Fe3, Fe4) = (−5/2, +4/2, +5/2), for which

the total spin is 2.

To identify the optimal spin states of the [3Fe-4S] medial cluster in the reduced and

oxidized states, *ab initio* electronic structure calculations were performed to obtain the

total energy values of Model(m) with various possible spin assignments (Table 3.1).

(a)	Fe1	Fe3	Fe4
[2, −2, 5]	1/2	−1/2	4/5
[5, −2, 2]	4/2	−1/2	1/2
[2, 5, −2]	1/2	4/2	−1/2
[−2, 5, 2]	−1/2	4/2	1/2
[5, 2, −2]	4/5	1/2	−1/2
[5, 4, −4]	4/2	3/2	−3/2
[5, −4, 4]	4/2	−3/2	3/2
[4, 5, −4]	3/2	4/2	-3/2
[−4, 5, 4]	−3/2	4/2	3/2
[4, −4, 5]	3/2	−3/2	4/2
[−4, 4, 5]	−3/2	3/2	4/2
[−6, 5, 6]	−5/2	4/2	5/2
[−6, 6, 5]	−5/2	5/2	4/2
[5, −6, 6]	4/2	−5/2	5/2
[5, 6, −6]	4/2	5/2	−5/2
[6, −6, 5]	5/2	−5/2	4/2
[6, 5, −6]	5/2	4/2	−5/2
[3, 2, 2]	2/2	1/2	1/2
[2, 3, 2]	1/2	2/2	1/2
[2, 2, 3]	1/2	1/2	2/2
[6, 4, −5]	5/4	3/2	−4/2
[4, 6, −5]	3/2	5/4	−4/2
[6, −5, 4]	5/4	−4/2	3/2
[4, −5, 6]	3/2	−4/2	5/4
[−5, 6, 4]	-4/2	5/4	3/2
[4, 6, −5]	3/2	5/4	−4/2
[1, 6, −2]	0	5/4	−3/2
[1, −2, 6]	0	−3/2	5/4
[6, 1, −2]	5/4	0	−3/2
[−2, 1, 6]	−3/2	0	5/4
[6, −2, 1]	5/4	−3/2	0
[−2, 6, 1]	−3/2	5/4	0

(b)	Fe1	Fe3	Fe4
[2, 2, −2]	1/2	1/2	−1/2
[2, −2, 2]	1/2	−1/2	1/2
[−2, 2, 2]	−1/2	1/2	1/2
[2, 4, −4]	1/2	3/2	−3/2
[2, −4, 4]	1/2	−3/2	3/2
[4, 2, −4]	3/2	1/2	−3/2
[−4, 2, 4]	−3/2	1/2	3/2
[4, −4, 2]	3/2	−3/2	1/2
[−4, 4, 2]	−3/2	3/2	1/2
[2, 6, −6]	1/2	5/2	−5/2
[2, −6, 6]	1/2	−5/2	5/2
[6, 2, −6]	5/2	1/2	-5/2
[−6, 2, 6]	−5/2	1/2	5/2
[6, −6, 2]	5/2	−5/2	1/2
[−6, 6, 2]	−5/2	5/2	1/2
[4,−2, −2]	3/2	−1/2	−1/2
[−2, 4, −2]	−1/2	3/2	−1/2
[−2, −2, 4]	−1/2	−1/2	3/2
[6,−4,−2]	5/2	−3/2	−1/2
[6,−2,−4]	5/2	−1/2	−3/2
[−4, 6, −2]	−3/2	5/2	-1/2
[−2, 6, −4]	−1/2	5/2	−3/2
[−2, −4, 6]	−1/2	−3/2	5/2
[−4, −2, 6]	−3/2	−1/2	5/2

Table 3.1. Possible spin states that were assigned to the [3Fe-4S] core of the medial cluster. The numbers of spin states analyzed are (a) 33 and (b) 24 types in the reduced and oxidized states, respectively. $S = 2$ and $S = 1/2$ were imposed as the total spin in the reduced and oxidized states, respectively.

3-2-3 Spin combination of the iron-sulfur clusters.

For the calculation of the fused model, Msspin(m), which is one of the most stable spin states of the medial cluster in the reduced state, was commonly used to the medial cluster, in Model(mp) 1 and 2. To the proximal clusters in Model(mp) 1 and 2, BS12 and BS34, which are the most stable spin state of the proximal cluster in the super-oxidized state, were assigned, respectively (see section 2-3-1 and 3-3-1).

For the calculation, total spin should be up spin. The spin of the medial cluster in the reduced state is 2 and the proximal cluster in the super-oxidized state is 1/2.[28] Therefore, to assign a spin state to the proximal cluster and the medial cluster, the spin of the proximal cluster must be up spin and the medial cluster is up or down spin. Therefore, we made four possible spin combinations, BS12(down) with Msspin(m)(up), BS12(up) with Msspin(m), BS34(down) with Msspin(m)(up), and BS34(up) with Msspin(m)(up). (up/down) means a direction of the spin.

3-2-4 Quantum mechanics calculation

All the *ab initio* electronic structure calculations were performed by employing Gaussian16,[56] and the all-electron hybrid spin-unrestricted Hartree-Fock (UHF)/density functional theory (DFT) scheme was adopted with the B3LYP functional.[31,32] In terms

of Fe and the atoms that directly coordinate to the Fe ions, triple-ζ valence polarized (TZVP) basis set [33,34] was applied. For the rest atoms, the 6-311G** basis set [35] was employed. For *ab initio* calculations of Model(m), geometry optimization was performed with all hydrogen atoms being movable.[36] For Model(mp), where the reduced states and the super-oxidized state were imposed to the proximal and medial clusters, respectively, the SCF calculations were performed.

3-3 Results and Discussion

3-3-1 Exploration of optimum spin assignment of Fe ions in [3Fe-4S] cluster

With respect to all the possible spin assignments of Model(m) in the reduced and oxidized states (Table 3.1), we calculated the potential energy values employing *ab initio* electronic structure calculation.

In the reduced state, the calculations were not converged in terms of the following five spin states, i.e., [5, 2, −2], [5, −2, 2], [2, −2, 5], [−2, 2, 5],[2, 3, 2], [2, 2, 3], [1, 6, −2], [1, −2, 6], [6, 1, −2], and [6, −2, 1], which would show that these spin states are unfavorable for Model(m) (Figure 3.3a). For the other cases, we evaluated the total energies, and found that the following seven spin states, i.e., [−4, 5, 4], [4, −4, 5], [−4, 4, 5], [−6, 5, 6], [−6, 6, 5], [−5, 6, 4], [−5, 4, 6], and [−2, 6, 1] were lower than the spin state [5, 4, −4] (note here that the total energy of the latter spin state was employed as the standard value for comparing the energy values of the reduced state), by 6.75 kcal/mol, in the energy value. This means that the resultant wave functions were identical in terms of those seven spin states. This calculation data are very strange, and must be explained.

So, we analyzed the processes of the SCF calculations. Prior to the SCF calculation

of the medial cluster in terms of each assigned spin combinations, a trial wave function was provided as the initial guess for the SCF iterations, by employing the algorithm implemented in Gaussian16. The above-mentioned six spin combinations, for which the SCF calculations were converged, were theoretically-possible spin combinations. However, the initial wave functions that were provided prior to the SCF calculations as the initial guess were found to be all identical (i.e., the identical coefficient values of the atomic orbitals for the wave function were assigned with respect to all six cases). As a result of the SCF calculations, the identical wave functions were obtained. This means that these spin assignments given as the initial states would be too unstable; in other words, the present system could be too restricted in the spin assignments, although further analyses are required to confirm it (Figure 3.3).

In the oxidized state, the SCF calculations were not converged with respect to the following ten spin states, i.e., [2, 2, −2], [2, −2, 2], [2, −4, 4], [4, −4, 2] [2, 6, −6], [−2, 4, −2], [−2, −2, 4], [−4, 6, −2], [−2, −4, 6] and [6, −4, −2], which would show that these spin states are unfavorable for Model(m) (Figure 3.3b). For the other cases, we evaluated the total energies, and found that the spin state [2, −6, 6] was lower than the spin state [−2, 2, 2] (the total energy of the latter spin state was employed as the standard value for comparing the energy values of the oxidized state), at least by 7.37kcal/mol, in the energy value. Thus, we concluded that [2, −6, 6] is most stable (Figure 3.3b).
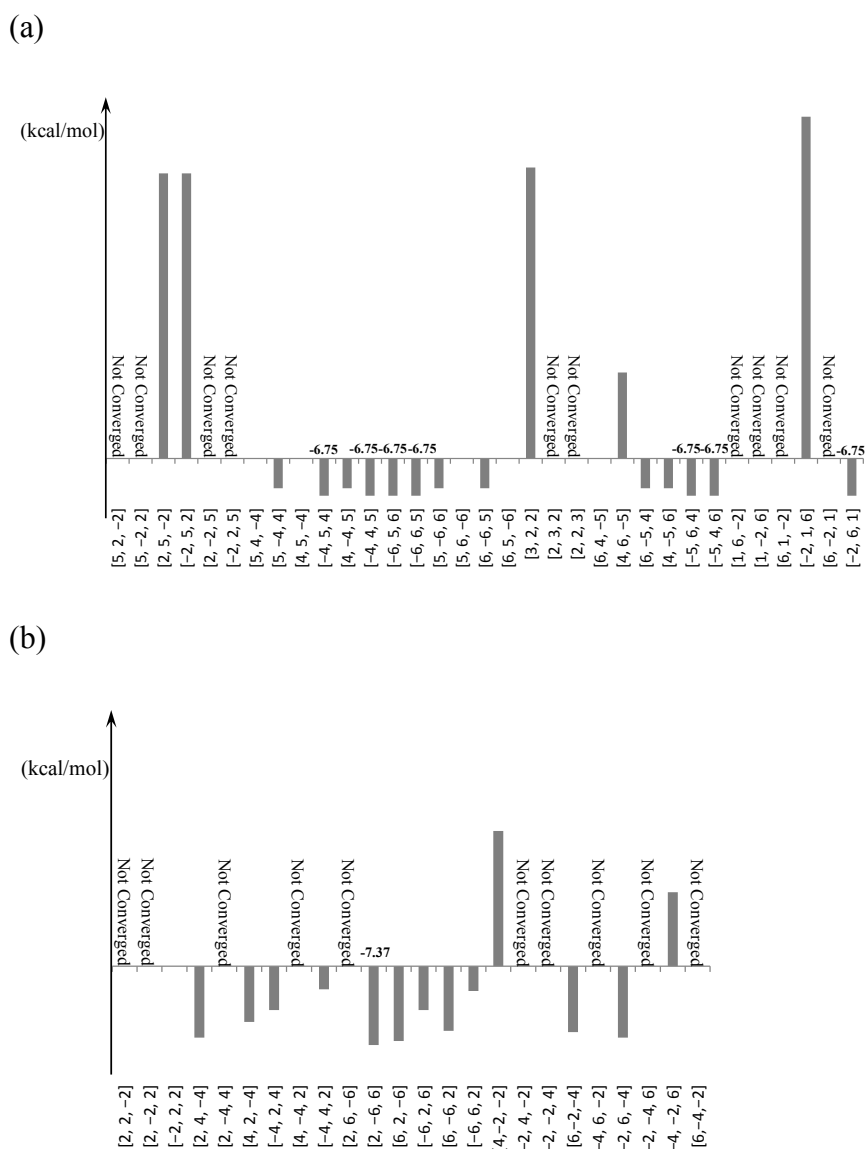
(a)

(b)

Figure 3.3. Total energy values of distinct 33 and 25 types of spin assignments in the reduced and oxidized states, respectively, where the energy values of the spin states of [5, 4, −4] and [−2, 2, 2] were employed as the reference energy values (i.e., 0 kcal/mol) in the reduced and oxidized states, respectively. In (a) the reduced state, [−4, 5, 4], [4, −4, 5], [−4, 4, 5], [−6, 5, 6], [−6, 6, 5], [−5, 6, 4], [−5, 4, 6], and [−2, 6, 1] are identical in the total energy (see text). In (b) the oxidized state, [2, −6, 6] is the most favorable spin state.

In this manner, we obtained stable spin states for the reduced and oxidized states of the medial cluster, and employed the combinations of these spin assignments as those of Model(mp).

3-3-2 Exploration of optimum spin combination of the fused model

We performed SCF calculation with respect to four possible combinations of spin directions. BS34(down) with [−6, 5, 6](up), which corresponds to Msspin(m), shows the lowest energy in four spin combinations. Three spin combinations, BS12(down) with [−6, 5, 6](up), BS12(up) with [−6, 5, 6](up), and BS34(down) with [−6, 5, 6](up), are comparable. The energy difference among three combinations is less than −2.56 kcal/mol. However, BS34(up) with [−6, 5, 6](up) spin combination is ~14.5 kcal/mol higher than other three spin combinations. Therefore we investigated three spin combinations except for BS34(up) with [−6, 5, 6](up).

3-3-3 Electronic structure analysis

We investigated electronic structures of the above-mentioned three different combinations of spin direct with the respect to model(mp) 1 and 2. As a result, we found identical orbitals with orbitals of the isolated proximal cluster and medial cluster, respectively. In Model(mp) 1, HOMO in BS12(down) with [−6, 5, 6](up) and HOMO in BS12(up) with [−6, 5, 6](up) are almost identical with the HOMO of Model 2 in BS12, respectively (see section 2-3-2). LUMO in BS12(down) with [−6, 5, 6](up) is almost identical MO231α of the medial cluster in [−6, 5, 6]. LUMO in BS12(up) with [−6, 5, 6](up) is almost identical MO224β of the medial cluster in [−6, 5, 6]. Moreover, we found that MO523α in BS12(down) with [−6, 5, 6](up) and MO519α in BS12(up) with

[−6, 5, 6](up) are identical with LUMO of Model 2 in BS12. The HOMO-LUMO energy gap in BS12(down) with [−6, 5, 6](up) and BS12(up) with [−6, 5, 6](up) are 24.64 kcal/mol and 7.35 kcal/mol, respectively.

In Model(mp) 2, HOMO in BS34(down) with [−6, 5, 6](up) is almost identical with the HOMO of Model 2 in BS34. LUMO in BS34(down) with [−6, 5, 6](up) is almost identical with MO231α of the medial cluster in [−6, 5, 6]. Moreover, we found that MO523α in BS34(down) with [−6, 5, 6](up) is identical with LUMO of Model 2 in BS34. The HOMO-LUMO energy gap in BS34(down) with [−6, 5, 6](up) is 27.27 kcal/mol.

Chapter 4
Future Perspectives

In this Chapter, we discuss some perspectives of the present study, that should be performed in the near future. The present study can provide a solid basis based on the substantial aspects relevant to the electronic structures, to elucidate the mechanisms of O_2-tolerant catalytic reaction cycle of hydrogenases. To consider such features, we need to possess unified viewpoints of structural molecular biology, quantum mechanics/ chemistry, and computer simulation analysis.

In the crystallographic data of MBHs, some amino acid residues around the proximal cluster exhibited multiple conformations, for which the meanings are still unknown. To resolve them, we need to perform three-dimensional (3D) geometrical and electronic structure analyses employing hybrid *ab initio* quantum mechanics/molecular mechanics (QM/MM) calculations. For this analysis, we should couple the calculations with long time-scale molecular dynamics (MD) simulations, which enables us to clarify the detailed energetics and functional roles that are relevant to those multiple conformations. This type of projects is also on-going in our group.

As described in the previous chapter, four types of spin combinations were investigated in the present analysis, adopting the most stable spin assignments that were revealed by *ab initio* calculations of the isolated proximal or medial cluster, as a preliminary examination (Calculations 1-4). However, other various spin combinations of the proximal and medial clusters are to be explored in the nearest future. Moreover,

we need to consider the environmental effects from the hydrogenase structures and the solvent water molecules, in our *ab initio* electronic structure calculations. For this aim, hybrid *ab initio* QM/MM calculations coupled with long time-scale molecular dynamics (MD) simulations are on-going in our group (Figure 4.1). Such an analysis can elucidate mechanisms of "communications" by the functional clusters in the reaction cycle.
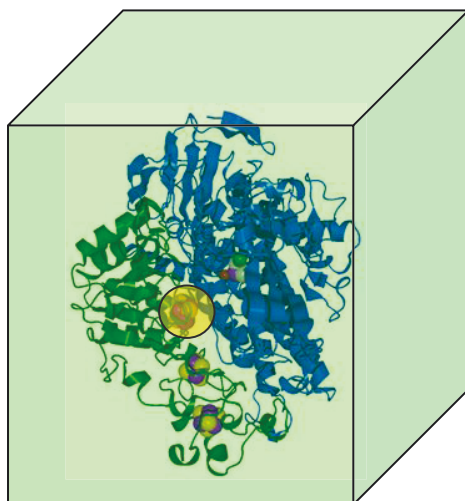

Figure 4.1. Structural model for our hybrid QM/MM calculation including the explicit solvent water molecules. The QM region (yellow circle) is composed of the [4Fe-3S] proximal cluster, i.e., His229, Glu76, Ser21 Cys115, Cys120, Cys149, Cys17, Cys19, Cys20, the hydroxyl ion, and two water molecules. The MM region is composed of all the rest of the protein structure, crystal water except for ones including the QM region, and the solvent water.

As shown in Chapter 2, the attachment of the hydroxyl ion induces the delocalization of the LUMOs, and thus makes a bridge between the proximal cluster and the [NiFe] active site, which may promote the ET between these two functional clustes. This should further be examined by estimating the relevant kinetic factors such as the re-organization energy[2] in the ET rates, k_{ET} (see section 2-2-5), which is on-going in our group with the use of hybrid *ab initio* QM/MM calculations of the entire enzyme with the explicit solvent water molecules.

From a technical point of view, it is interesting that the present *ab initio* calculations employing the B3LYP functional should be evaluated employing more advanced QM methodologies in the nearest future, although this functional has been shown to work in an extremely broad range of materials up to date. In fact, with respect to the [NiFe] active site, it was reported that the B3LYP functional significantly underestimated the total energy values,[50] while for the proximal cluster, it reportedly worked well.[21,43] Furthermore, the orbital analysis performed in the present study should further be examined by employing the re-constituted orthogonal orbitals, such as the Wannier function,[51,52] which is also on-going in our group.

References

1) M. Stephenson and L. H. Stickland, Biochem. J. **25**, 215 (1931).

2) M. Stephenson and L. H. Stickland, Biochem. J. **25**, 205 (1931).

3) A. K. Jones, E. Sillery, S. P. Albracht, and F. A. Armstrong, Chem. Commun. **8**, 866 (2002).

4) A. Le Goff, V. Artero, B. Jousselme, P. D. Tran, N. Guillet, R. Metaye, A. Fihri, S. Palacin, and M. Fontecave, Science **326**, 1384 (2009).

5) S. T. Stripp, G. Goldet, C. Brandmayr, O. Sanganas, K. A. Vincent, M. Haumann, F. A. Armstrong, and T. Happe, Proc. Natl. Acad. Sci. U.S.A. **106**, 17331 (2009).

6) R. Sathre, C. D. Scown, W. R. Morrow, III, J. C. Stevens,I. D. Sharp, J. W. Ager, III, K. Walczak, F. A. Houle, and J. B. Greenblatt, Energy Environ. Sci. **7**, 3264 (2014).

7) B. Friedrich, J. Fritsch, and O. Lenz, Curr. Opin. Biotechnol. **22**, 358 (2011).

8) K. A. Vincent, J. A. Cracknell, J. R. Clark, M. Ludwig, O. Lenz, B. Friedrich, and F. A. Armstrong, Chem. Commun. **48**, 5033 (2006).

9) P. M. Vignais and B. Billoud, Chem. Rev. **107**, 4206 (2007).

10) T. Yagi and Y. Higuchi, Proc. Jpn. Acad., Ser. B, Phys. Biol. Sci. **89**, 16 (2013).

11) W. Lubitz, H. Ogata, O. Rudiger, and E. Reijerse, Chem. Rev. **114**, 4081 (2014).

12) A more detailed discussion is given in Supplemental Material.

13) G. Goldet, C. Brandmayr, S. T. Stripp, T. Happe, C. Cavazza, J. C. Fontecilla-Camps, and F. A. Armstrong, J. Am. Chem. Soc. **131**, 14979 (2009).

14) S. Shima and R. K. Thauer, Chem. Rec. **7**, 37 (2007).

15) A. Volbeda, P. Amara, C. Darnault, J. M. Mouesca, A. Parkin, M. M. Roessler, F. A. Armstrong, and J. C. Fontecilla-Camps, Proc. Natl. Acad. Sci. U.S.A. **109**, 5305 (2012).

16) J. Fritsch, O. Lenz, and B. Friedrich, Nat. Rev. Microbiol. **11**, 106 (2013).

17) K. A. Vincent, A. Parkin, and F. A. Armstrong, Chem. Rev. **107**, 4366 (2007).

18) J. C. Fontecilla-Camps, A. Volbeda, C. Cavazza, and Y. Nicolet, Chem. Rev. **107**, 4273 (2007).

19) Y. Shomura, K. S. Yoon, H. Nishihara, and Y. Higuchi, Nature **479**, 253 (2011).

20) J. Fritsch, P. Scheerer, S. Frielingsdorf, S. Kroschinsky, B. Friedrich, O. Lenz, and C. M. Spahn, Nature **479**, 249 (2011).

21) S. Frielingsdorf, J. Fritsch, A. Schmidt, M. Hammer, J. Lowenstein, E. Siebert, V. Pelmenschikov, T. Jaenicke, J. Kalms, Y. Rippers, F. Lendzian, I. Zebger, C. Teutloff, M. Kaupp, R. Bittl, P. Hildebrandt, B. Friedrich, O. Lenz, and P. Scheerer, Nat. Chem. Biol. **10**, 378 (2014)

22) T. Goris, A. F. Wait, M. Saggu, J. Fritsch, N. Heidary, M. Stein, I. Zebger, F. Lendzian, F. A. Armstrong, B. Friedrich, and O. Lenz, Nat. Chem. Biol. **7**, 310 (2011).

23) M. E. Pandelia, W. Nitschke, P. Infossi, M. T. Giudici-Orticoni, E. Bill, and W. Lubitz, Proc. Natl. Acad. Sci. U.S.A. **108**, 6097 (2011).

24) A. Parkin and F. Sargent, Curr. Opin. Biotechnol. **16**, 26 (2012).

25) E. Siebert, Y. Rippers, S. Frielingsdorf, J. Fritsch, A. Schmidt, J. Kalms, S. Katz, O. Lenz, P. Scheerer, L. Paasche, V. Pelmenschikov, U. Kuhlmann, M. A. Mroginski, I. Zebger, and P. Hildebrandt, J. Phys. Chem. B **119**, 13785 (2015).

26) I. Dance, Chem. Sci. **6**, 1433 (2015).

27) L. Noodleman and D. A. Case, Adv. Inorg. Chem. **38**, 423 (1992).

28) M. E. Pandelia, D. Bykov, R. Izsak, P. Infossi, M. T. Giudici-Orticoni, E. Bill, F. Neese, and W. Lubitz, Proc. Natl. Acad. Sci. U.S.A. **110**, 483 (2013).

29) R. Grajczyk, R. Berthelot, S. Muir, A. W. Sleight, and M. A. Subramanian, J. Solid State Chem. **199**, 102 (2013).

30) M. J. Frisch, G. W. Trucks, H. B. Schlegel, G. E. Scuseria, M. A. Robb, J. R. Cheeseman, G. Scalmani, V. Barone, B. Mennucci, G. A. Petersson, H. Nakatsuji, M. Caricato, X. Li, H. P. Hratchian, A. F. Izmaylov, J. Bloino, G. Zheng, J. L. Sonnenberg, M. Hada, M. Ehara, K. Toyota, R. Fukuda, J. Hasegawa, M. Ishida, T. Nakajima, Y. Honda, O. Kitao, H. Nakai, T. Vreven, J. A. Montgomery, Jr., J. E. Peralta, F. Ogliaro, M. Bearpark, J. J. Heyd, E. Brothers, K. N. Kudin, V. N. Staroverov, R. Kobayashi, J. Normand, K. Raghavachari, A. Rendell, J. C. Burant, S. S. Iyengar, J. Tomasi, M. Cossi, N. Rega, J. M. Millam, M. Klene, J. E. Knox, J. B. Cross, V. Bakken, C. Adamo, J. Jaramillo, R. Gomperts, R. E. Stratmann, O. Yazyev, A. J. Austin, R. Cammi, C. Pomelli, J. W. Ochterski, R. L. Martin, K. Morokuma, V. G. Zakrzewski, G. A. Voth, P. Salvador, J. J. Dannenberg, S. Dapprich, A. D. Daniels, Ö. Farkas, J. B. Foresman, J. V. Ortiz, J. Cioslowski, and D. J. Fox, Revision C.01, Gaussian, Inc., Wallingford CT, 2009.

31) C. Lee, W. Yang, and R. G. Parr, Phys. Rev. B **37**, 785 (1988).

32)   A. D. Becke, Phys. Rev. A **38**, 3098 (1988).

33)   A. Schäfer, H. Horn, and R. Ahlrichs, J. Chem. Phys. **97**, 2571 (1992).

34)   A. Schäfer, C. Huber, and R. Ahlrichs, J. Chem. Phys. **100**, 5829 (1994).

35)   A. D. McLean and G. S. Chandler, J. Chem. Phys. **72**, 5639 (1980).

36)   I. A. Balabin, X. Hu, and D. N. Beratan, J. Comput. Chem. **33**, 906 (2012).

37)   D. N. Beratan, J. N. Betts, and J. N. Onuchic, Science **252**, 1285 (1991).

38)   R. A. Marcus and N. Sutin, Biochim. Biophys. Acta **811**, 265 (1985).

39)   G. L. Closs and J. R. Miller, Science **240**, 440 (1988).

40)   M. L. Jones, I. V. Kurnikov, and D. N. Beratan, J. Phys. Chem. A **106**, 2002 (2002).

41)   H. Beinert, R. H. Holm, and E. Munck, Science **277**, 653 (1997).

42)   V. Pelmenschikov and M. Kaupp, J. Am. Chem. Soc. **135**, 11809 (2013).

43)   V. Radu, S. Frielingsdorf, O. Lenz, and L. J. Jeuken, Chem. Commun. **52**, 2632 (2016).

44)   K. Knüttel, K. Schneider, W. Plass, A. Muller, E. Bill, A. X. Trautwein, and A. Erken, Bull. Pol. Acad. Sci. Chem. **42**, 495 (1994).

45)   M. M. Roessler, R. M. Evans, R. A. Davies, J. Harmer, and F. A. Armstrong, J. Am. Chem. Soc. **134**, 15581 (2012).

46)   J. M. Mouesca, J. C. Fontecilla-Camps, and P. Amara, Angew. Chem. Int. Ed. **52**, 2002 (2013).

47)   J. Kang, H. Kino, and M. Tateno, Biochim. Biophys. Acta **1807**, 1314 (2011).

48)   H. S. Shafaat, O. Rudiger, H. Ogata, and W. Lubitz, Biochim. Biophys. Acta **1827**, 986 (2013).

49)   P. Wulff, C. Thomas, F. Sargent, and F. A. Armstrong, J. Biol. Inorg. Chem. **21**, 121 (2016).

50)   A. Volbeda, C. Darnault, A. Parkin, F. Sargent, F. A. Armstrong, and J. C. Fontecilla-Camps, Structure **21**, 184 (2013).

51)   S. Kurkin, S. J. George, R. N. Thorneley, and S. P. Albracht, Biochemistry **43**, 6820 (2004).

52)   G. Dong, Q. M. Phung, S. D. Hallaert, K. Pierloot, and U. Ryde, Phys. Chem. Chem. Phys. **19**, 10590 (2017).

53)   G. H. Wannier, Phys. Rev. **52**, 191 (1937).

54) S. F. Boys, Rev. Mod. Phys. **32**, 296 (1960).

55) J. Kim, J. Kang, H. Nishigami, H. Kino, M. Tateno, J. Phys. Soc. Jpn. (2018)

56) Gaussian 16, Revision A.03, M. J. Frisch, G. W. Trucks, H. B. Schlegel, G. E. Scuseria, M. A. Robb, J. R. Cheeseman, G. Scalmani, V. Barone, G. A. Petersson, H. Nakatsuji, X. Li, M. Caricato, A. V. Marenich, J. Bloino, B. G. Janesko, R. Gomperts, B. Mennucci, H. P. Hratchian, J. V. Ortiz, A. F. Izmaylov, J. L. Sonnenberg, D. Williams-Young, F. Ding, F. Lipparini, F. Egidi, J. Goings, B. Peng, A. Petrone, T. Henderson, D. Ranasinghe, V. G. Zakrzewski, J. Gao, N. Rega, G. Zheng, W. Liang, M. Hada, M. Ehara, K. Toyota, R. Fukuda, J. Hasegawa, M. Ishida, T. Nakajima, Y. Honda, O. Kitao, H. Nakai, T. Vreven, K. Throssell, J. A. Montgomery, Jr., J. E. Peralta, F. Ogliaro, M. J. Bearpark, J. J. Heyd, E. N. Brothers, K. N. Kudin, V. N. Staroverov, T. A. Keith, R. Kobayashi, J. Normand, K. Raghavachari, A. P. Rendell, J. C. Burant, S. S. Iyengar, J. Tomasi, M. Cossi, J. M. Millam, M. Klene, C. Adamo, R. Cammi, J. W. Ochterski, R. L. Martin, K. Morokuma, O. Farkas, J. B. Foresman, and D. J. Fox, Gaussian, Inc., Wallingford CT, 2016.

Acknowledgements